Real-time 3-D modeling of the ground electric field due to space weather events. A concept and its validation

Mikhail Kruglyakov[1,2], **Alexey Kuvshinov**[3], **Elena Marshalko**[4,5,6]

[1]University of Otago, Dunedin, New Zealand
[2]Geoelectromagnetic Research Center, Institute of Physics of the Earth, Moscow, Russia
[3]Institute of Geophysics, ETH Zürich, Zürich, Switzerland
[4]Institute of Physics of the Earth, Moscow, Russia
[5]Geophysical Center, Moscow, Russia
[6]Finnish Meteorological Institute, Helsinki, Finland

Key Points:

- We present the formalism of real-time modeling of the ground electric field (GEF) excited by temporally and spatially varying source
- The formalism relies on the factorization of the source and exploits precomputed frequency-domain GEF
- Using Fennoscandia as a test region, we show that real-time 3-D modeling of the GEF takes less than 0.025 seconds

Corresponding author: Mikhail Kruglyakov, m.kruglyakov@gmail.com

Abstract

We present a methodology that allows researchers to simulate in real time the spatiotemporal dynamics of the ground electric field (GEF) in a given 3-D conductivity model of the Earth based on continuously augmented data on the spatiotemporal evolution of the inducing source. The formalism relies on the factorization of the source by spatial modes and time series of respective expansion coefficients and exploits precomputed frequency-domain GEF generated by corresponding spatial modes. To validate the formalism, we invoke a high-resolution 3-D conductivity model of Fennoscandia and consider a realistic source built using the Spherical Elementary Current Systems (SECS) method as applied to magnetic field data from the IMAGE network of observations. The factorization of the SECS-recovered source is then performed using the principal component analysis. Eventually, we show that the GEF computation at a given time instant on a 512×512 grid requires less than 0.025 seconds provided that frequency-domain GEF due to pre-selected spatial modes are computed in advance. Taking the 7-8 September 2017 geomagnetic storm as a space weather event, we show that real-time high-resolution 3-D modeling of the GEF is feasible. This opens a practical opportunity for GEF (and eventually geomagnetically induced currents) nowcasting and forecasting.

Plain Language Summary

The solar activity in the form of coronal mass ejections leads to abnormal fluctuations of the geomagnetic field. These fluctuations, in their turn, generate so-called geomagnetically induced currents (GIC) in electric power grids, which may pose a significant risk to the reliability and durability of such infrastructure. Forecasting GIC is one of the grand challenges of the modern space weather studies. One of the critical components of such forecasting is real-time simulation of the ground electric field (GEF), which depends on the electrical conductivity distribution inside the Earth and the spatiotemporal structure of geomagnetic field fluctuations. In this paper, we present and validate a methodology that allows researchers to simulate the GEF in fractions of a second (thus, in real time) irrespective of the complexity of the Earth's conductivity and geomagnetic field fluctuations models.

1 Introduction

As commonly recognized, geomagnetically induced currents (GIC) in electric power grids may pose a significant risk to the reliability and durability of such infrastructure (Bolduc, 2002; Love et al., 2018).

The ultimate goal of quantitative estimation of the hazard to power grids from abnormal geomagnetic disturbances (space weather events) is real-time and as realistic as practicable forecasting of GIC. Under GIC forecasting, we understand the time-domain computation of GIC using continuously augmented data on the spatiotemporal evolution of the source responsible for the geomagnetic disturbances. Specifically, to forecast GIC in the region of interest, one needs: (1) to adequately parameterize the source of geomagnetic disturbances; (2) to forecast the spatiotemporal evolution of the source in the region; (3) to specify/build a three-dimensional (3-D) electrical conductivity model of the Earth's subsurface; (4) to perform real-time modeling of the ground electric field (GEF) in a given 3-D conductivity model, i.e., to compute as fast as feasible the spatiotemporal progression of the GEF from continuously augmented data on the spatiotemporal evolution of the forecasted source; (5) to convert the "forecasted" GEF into GIC.

It is well accepted that the decades of satellite observations of the solar wind parameters (plus observations of interplanetary magnetic field) at the L1 Lagrangian point are the most promising data for forecasting spatiotemporal evolution of the source with algorithms known as neural networks (NN). Despite numerous studies that attempt to

forecast the source evolution using different NN architectures quantitatively, the progress here is rather limited. This is, in particular, because the full potential of NN remains unexplored; the reader can find a rather exhaustive review of the literature on the subject in Tasistro-Hart et al. (2021). But even if the source forecasting will be feasible in the future, with the measurements at the L1 point, it is nearly impossible to forecast the source more than an hour in advance. This, in particular, means that forecasting GEF in a given 3-D conductivity model from continuously augmented data on the spatiotemporal evolution of the forecasted source should be performed "on the fly", i.e., within a few seconds, if one wishes to approach an ultimate goal of GIC forecasting in the region of interest – development of trustful alerting systems for the power industry. Note that once the GEF is forecasted, a conversion of the GEF into GIC is rather straightforward (Kelbert, 2020) and requires fractions of seconds provided the geometry of transmission lines and system design parameters are granted by power companies.

This paper presents and validates a methodology that allows researchers to simulate the spatiotemporal progression of the GEF in a 3-D conductivity model "on the fly". The paper also discusses how the concept can be exploited for GEF nowcasting and forecasting.

2 Methodology

2.1 Governing equations in the frequency domain

We start with the discussion of the problem in the frequency domain. Maxwell's equations govern electromagnetic (EM) field variations, and in the frequency domain, these equations are read as

$$\frac{1}{\mu_0}\nabla\times\mathbf{B} = \sigma\mathbf{E}+\mathbf{j}^{\text{ext}}, \tag{1}$$

$$\nabla\times\mathbf{E} = \mathrm{i}\omega\mathbf{B}, \tag{2}$$

where μ_0 is the magnetic permeability of free space; ω is angular frequency; $\mathbf{j}^{\text{ext}}(\mathbf{r},\omega)$ is the extraneous (inducing) electric current density; $\mathbf{B}(\mathbf{r},\omega;\sigma),\mathbf{E}(\mathbf{r},\omega;\sigma)$ are magnetic and electric fields, respectively. $\sigma(\mathbf{r})$ is the spatial distribution of electrical conductivity, $\mathbf{r}=(r,\vartheta,\varphi)$ a position vector, either in the spherical or Cartesian coordinates. Note that we neglected displacement currents and adopt the following Fourier convention

$$f(t)=\frac{1}{2\pi}\int\limits_{-\infty}^{\infty} f(\omega)e^{-\mathrm{i}\omega t}\mathrm{d}\omega. \tag{3}$$

Note that we will use the same notation for the fields in the time and frequency domain. We also assume that the current density, $\mathbf{j}^{\text{ext}}(\mathbf{r},\omega)$, can be represented as a linear combination of spatial modes $\mathbf{j}_i(\mathbf{r})$,

$$\mathbf{j}^{\text{ext}}(\mathbf{r},\omega) = \sum_{i=1}^{L} c_i(\omega)\mathbf{j}_i(\mathbf{r}). \tag{4}$$

Note that the form of spatial modes $\mathbf{j}_i(\mathbf{r})$ (and their number, L) varies with application. For example, $\mathbf{j}^{\text{ext}}(\mathbf{r},\omega)$ is parameterized via spherical harmonics (SH) in Püthe and Kuvshinov (2013); Honkonen et al. (2018); Guzavina et al. (2019); Grayver et al. (2021), current loops in Sun and Egbert (2012), or eigenmodes from the Principal component analysis (PCA) of the physics-based models in Egbert et al. (2021) and Zenhausern et al. (2021).

By virtue of the linearity of Maxwell's equations with respect to the $\mathbf{j}^{\text{ext}}(\mathbf{r},\omega)$ term, we can expand the total (i.e., inducing plus induced) electric field as a linear combina-

tion of individual fields $\mathbf{E}_i$,

$$\mathbf{E}(\mathbf{r},\omega;\sigma) = \sum_{i=1}^{L} c_i(\omega)\mathbf{E}_i(\mathbf{r},\omega;\sigma), \tag{5}$$

where the $\mathbf{E}_i(\mathbf{r},\omega;\sigma)$ field is the "electric" solution of the following Maxwell's equations:

$$\frac{1}{\mu_0}\nabla\times\mathbf{B}_i = \sigma\mathbf{E}_i + \mathbf{j}_i, \tag{6}$$

$$\nabla\times\mathbf{E}_i = \mathrm{i}\omega\mathbf{B}_i. \tag{7}$$

2.2 Governing equations in the time domain

The transformation of the Equation (5) into the time domain leads to the representation of the time-varying ground electric field as convolution integrals

$$\mathbf{E}(\mathbf{r}_s,t;\sigma) = \sum_{i=1}^{L}\int_{-\infty}^{t} c_i(\tau)\mathbf{E}_i(\mathbf{r}_s,t-\tau;\sigma)\mathrm{d}\tau, \tag{8}$$

or equivalently

$$\mathbf{E}(\mathbf{r}_s,t;\sigma) = \sum_{i=1}^{L}\int_{0}^{\infty} c_i(t-\tau)\mathbf{E}_i(\mathbf{r}_s,\tau;\sigma)\mathrm{d}\tau, \tag{9}$$

where $\mathbf{r}_s$ stands for the position vector at the surface of the Earth. The reader is referred to Appendix A for more details on the convolution integrals in Equations (8) and (9).

Since the radial component of the GEF is negligibly small (due to insulating air) and is not used in GIC calculations (Kelbert, 2020), we will confine ourselves to forecasting of the horizontal electric field solely; thus, hereinafter, $\mathbf{E}_i$ will stand for $\mathbf{E}_i = (E_{x,i}\ E_{y,i})$.

2.3 Real-time modeling of the GEF. A concept

Equation (9) shows how the GEF can be modeled using continuously augmented data on the time evolution of the nowcasted or forecasted c_i (note that forecasting of the c_i is outside the scope of this paper). To make the formula ready for implementation, one needs: (a) to specify a set of spatial modes, $\mathbf{j}_i, i = 1,2,\ldots,L$ in the region, where GIC nowcasting/forecasting is required; we will discuss the construction of $\mathbf{j}_i$ in Section 3.1; (b) to set up a 3-D conductivity model in this region; and (c) to estimate an upper limit of integrals in Equation (9), or, in other words, to estimate a time interval, T, above which $\mathbf{E}_i(\mathbf{r}_s,\tau;\sigma)$ becomes negligibly small. The latter will allow us to rewrite Equation (9) as

$$\mathbf{E}(\mathbf{r}_s,t;\sigma) \approx \sum_{i=1}^{L}\int_{0}^{T} c_i(t-\tau)\mathbf{E}_i(\mathbf{r}_s,\tau;\sigma)\mathrm{d}\tau. \tag{10}$$

Note that the upper limit in the integrals could be different for different spatial modes, different components of the field, and different locations. However, one can choose a conservative approach, taking a single T irrespective of modes/components/locations as a maximum from all individual upper limit estimates. We will discuss the estimation of T in Sections 3.3 and 3.4 .

The details of numerical calculation of the integrals in (10) are presented in Appendix B. In short, assuming that $c_i(t), i = 1,2,\ldots,L$ are time series with the sampling interval Δt and $T = N_t\Delta t$, we approximate $\mathbf{E}(\mathbf{r}_s,t_k;\sigma)$ at $t_k = k\Delta t$ as

$$\mathbf{E}(\mathbf{r}_s,t_k;\sigma) \approx \sum_{i=1}^{L}\left\{\sum_{n=0}^{N_t} d_i(t_k,n\Delta t;T)\mathcal{M}^n_{\mathbf{E}_i}(\mathbf{r}_s;\sigma) + \left[c_i(t_k-T)-c_i(t_k)\right]\mathcal{L}_i\left(\mathbf{r}_s,T;\sigma\right)\right\}, \tag{11}$$

where d_i is defined as

$$d_i(t,\tau;T) = \begin{cases} c_i(t-\tau) - c_i(t) - \dfrac{c_i(t-T)-c_i(t)}{T}\tau, & \tau \in [0,T] \\ 0, & \tau \notin [0,T]. \end{cases} \tag{12}$$

The reasoning to represent time-dependent part in Equation (11) in this form is given in Appendix B. Note also that quantities $\mathcal{M}^n_{\mathbf{E}_i}(\mathbf{r}_s;\sigma)$ and $\mathcal{L}_i(\mathbf{r}_s,T;\sigma)$ are time-invariant, and for the given $\mathbf{j}_i$, $i = 1,2,\ldots,L$ and 3-D conductivity model are calculated only once, then stored and used, when the calculation of $\mathbf{E}(\mathbf{r}_s,t_k;\sigma)$ is required. Actual form and estimation for $\mathcal{M}^n_{\mathbf{E}_i}(\mathbf{r}_s;\sigma)$ and $\mathcal{L}_i(\mathbf{r}_s,T;\sigma)$ are also discussed in Appendix B.

Equation (11) is an essence of the real-time GEF calculation, showing that $\mathcal{O}(L \times N_t \times N_g)$ summations and multiplications are required at a (current) time instant t_k plus some overhead to read the precomputed $\mathcal{M}^n_{\mathbf{E}_i}(\mathbf{r}_s;\sigma)$ and $\mathcal{L}_i(\mathbf{r}_s,T;\sigma)$ from the disc. Note that N_g is a number of points $\mathbf{r}_s$, at which the GEF is computed.

3 Real-time modeling of the GEF. Validation of the concept

The validation of the presented concept will be performed using Fennoscandia as a test region. The choice of Fennoscandia is motivated by several reasons. First, it is a high-latitude region, where GIC are expected to be especially large. Second, there exists a 3-D electrical conductivity model of the region (Korja et al., 2002). Third, the regional magnetometer network (International Monitor for Auroral Geomagnetic Effect, IMAGE (Tanskanen, 2009), allows us to build a realistic model of the source. Finally, the last but not the least consideration to choose this region is the fact that we have already performed a comprehensive 3-D EM model study in this region (Marshalko et al., 2021).

3.1 Building a model of the source

First, let us rewrite Equation (4) in the time domain

$$\mathbf{j}^{\text{ext}}(\mathbf{r},t) = \sum_{i=1}^{L} c_i(t)\mathbf{j}_i(\mathbf{r}). \tag{13}$$

We will further assume that the extraneous current $\mathbf{j}^{\text{ext}}(\mathbf{r},t)$ is divergence-free, it flows in a thin layer at the altitude of $h = 90$ km, and this layer is separated from the Earth by the insulating atmosphere. Following the Spherical Elementary Current Systems (SECS) method (Vanhamäki & Juusola, 2020), this current is represented as

$$\mathbf{j}^{\text{ext}}(\mathbf{r},t) = \delta(r-R)\sum_{m=1}^{M} S_m(t)[P(\mathbf{r},\mathbf{r}_m)\mathbf{e}_\vartheta + Q(\mathbf{r},\mathbf{r}_m)\mathbf{e}_\varphi], \tag{14}$$

where δ is Dirac's delta function, $\mathbf{e}_\vartheta$ and $\mathbf{e}_\varphi$ are unit vectors of the spherical coordinate system, $\mathbf{r} = (R,\vartheta,\varphi)$, $\mathbf{r}_m = (R,\vartheta_m,\varphi_m)$, $R = a + h$, a is a mean radius of the Earth, $\mathbf{r}_m$ is the location of the pole of the m-th spherical elementary current system and S_m is the so-called scalar factor associated with the m-th pole. Expressions for $P(\mathbf{r},\mathbf{r}_m)$ and $Q(\mathbf{r},\mathbf{r}_m)$ are presented in Appendix D. Note that in practice $\mathbf{r}$ and $\mathbf{r}_m$ are usually taken as the nodes of two (similar) grids, which are slightly shifted with respect to each other (the reason for the shift is explained in Appendix D). Once $S_m(t)$, $m = 1 \ldots M$ are obtained by means of the SECS method as applied to some real data for some event, one can perform the PCA of $S_m(t)$ expecting that the spatial structure of $S_m(t)$ will be well approximated with a small number of modes v_i, $i = 1,2,\ldots L$ allowing to represent $\mathbf{j}_i$ as

$$\mathbf{j}_i(\mathbf{r}) = \delta(r-R)\sum_{m=1}^{M} v_i(\mathbf{r}_m)[P(\mathbf{r},\mathbf{r}_m)\mathbf{e}_\vartheta + Q(\mathbf{r},\mathbf{r}_m)\mathbf{e}_\varphi], \;\; i = 1,2,...,L. \tag{15}$$

The aim of this section is to obtain v_i and, consequently, $\mathbf{j}_i$ (using Equation 15). To this end, we apply the SECS method to 10-sec vector magnetic field data from all available (38) stations of the IMAGE network during the 7-8 September 2017 geomagnetic storm. Locations of IMAGE sites are shown in Figure 1. Considered (8-hours) time period is from 20:00:00 UT, September 7, 2017, to 03:59:50 UT, September 8, 2017, thus, including the onset and the main phase of the storm. S was estimated at $0.5^\circ \times 1^\circ$ grid of $21^\circ \times 38^\circ$ part of a sphere. Coordinates of the region are 59°N – 79°N and 4°E – 42°E. This set up, in particular, means that S was computed at $M = 42 \times 39 = 1638$ grid points and $N = 2880$ time instants. Note that the same event, region and grid were considered in our recent study (Marshalko et al., 2021).

The PCA of $S_m(t)$ is performed in a similar manner as it was done, for example, in Alken et al. (2017); Egbert et al. (2021); Zenhausern et al. (2021). Specifically, we construct a matrix F as

$$F = \begin{pmatrix} S_1^1 & S_2^1 & \cdots & S_M^1 \\ S_1^2 & S_2^2 & \cdots & S_M^2 \\ \vdots & \vdots & \ddots & \vdots \\ S_1^N & S_2^N & \cdots & S_M^N \end{pmatrix}, \tag{16}$$

where S_m^n is $S_m(t)$ estimated at the n-th time instant at the m-th grid point. Further, according to the PCA concept, we form an $M \times M$ covariance matrix R

$$R = F^T F, \tag{17}$$

and apply an eigenvalue decomposition to R

$$RV = V\Lambda, \tag{18}$$

where Λ is a diagonal matrix containing the eigenvalues $\lambda_i, i = 1, 2, ..., M$ of R. The v_i at M grid points is represented by i-th column vector of V which is in its turn the eigenvector of R corresponding to the eigenvalue λ_i. Both V and Λ are matrices of the size $M \times M$. The superscript T in Equation (17) denotes the transpose. The eigenvectors v_i represent the spatial modes (principal components; PCs), whereas the eigenvalues give the respective PC's variance contribution. The corresponding time series c_i are calculated as

$$c_i(t) = \sum_{m=1}^{M} S_m(t) v_i(\mathbf{r}_m). \tag{19}$$

PCs are usually sorted in order from the largest to the smallest eigenvalues. The PC corresponding to the largest eigenvalue will explain the most variance, followed by the second, third PC, etc... In practice, the PCs corresponding to a few of the largest eigenvalues explain most of the analyzed fields' variance. The cumulative variance of L PCs can be calculated as (Alken et al., 2017)

$$\kappa_L = \frac{\sum_{i=1}^{L} \lambda_i}{\sum_{i=1}^{M} \lambda_i}, \tag{20}$$

Figure 2 presents the cumulative variance for the first 30 spatial modes. Horizontal dashed line allows us to estimate the number of modes needed to explain 99 % of the spatial variability of $S_m(t)$. It is seen from the figure that one needs $L = 21$ spatial modes to explain most (99 %) of the variance. This is a dramatic reduction from the total $M = 1638$ spatial modes. These 21 modes will be used in the further discussion of the real-time calculation of the GEF. Figure 3 shows $\mathbf{j}_i$ corresponding to spatial modes of different i, illustrating the fact that the modes with larger i capture smaller spatial structures of the

source. The respective time series c_i are presented in Figure 4. Figure 5 compares the maps of the original and the PCA-based source for two snapshots of the enhanced geomagnetic activity. The original source is built using the SECS method (cf. Equation 14), whereas PCA-based source is calculated using Equations (13) and (15). It is seen that the agreement between the original and PCA-based sources is very good both in terms of the amplitude and spatial pattern. In addition, Figure 6 demonstrates the comparison of the time series of these sources for two exemplary sites (shown in Figure 5 as white circles): one is located in the region where the significant source current is observed (Jäckvik (JCK)), another – aside from this region (Tartu (TAR)). Again, we observe good agreement between the two sources, especially for the site above which the source current is large.

3.2 3-D conductivity model of Fennoscandia

We took the 3-D conductivity model of the region from Marshalko et al. (2021), where it was constructed using the SMAP (Korja et al., 2002) – a set of maps of crustal conductances (vertically integrated electrical conductivities) of the Fennoscandian Shield, surrounding seas, and continental areas. The SMAP consists of six layers of laterally variable conductance. Each layer has a thickness of 10 km. The first layer comprises contributions from the seawater, sediments, and upper crust. The other five layers describe conductivity distribution in the middle and lower crust. SMAP covers an area 0°E – 50°E and 50°N – 85°N and has $5' \times 5'$ resolution. We converted the original SMAP database into a Cartesian 3-D conductivity model of Fennoscandia with three layers of laterally variable conductivity of 10, 20, and 30 km thicknesses (cf. Figures 7a-c). This vertical discretization is chosen to be compatible with that previously used by Rosenqvist and Hall (2019) and Dimmock et al. (2019, 2020) for GIC studies in the region. Conductivities in the second and the third layer of this model are simple averages of the conductivities in the corresponding layers of the original conductivity model with six layers. To obtain the conductivities in Cartesian coordinates, we applied the transverse Mercator map projection (latitude and longitude of the true origin are 50°N and 25°E, correspondingly) to the original data, and then performed the interpolation to a laterally regular grid. The lateral discretization and the size of the resulting 3-D part of the conductivity model of Fennoscandia were taken as 5×5 km^2 and 2550×2550 km^2, respectively. Deeper than 60 km, we used the 1-D conductivity profile obtained by Kuvshinov et al. (2021) (cf. Figure 7d), which is an updated version of the 1-D profile from Grayver et al. (2017).

Note that the lateral discretization and the size of the conductivity model of Fennoscandia imply that the GEF is calculated at a grid comprising $N_g = 512 \times 512$ points.

3.3 Computation of $\mathbf{E}_i(\mathbf{r}_s, \omega; \sigma)$

As is seen from Equations (B13) and (C2) one needs to compute $\mathbf{E}_i(\mathbf{r}_s, \omega; \sigma)$ at a number of frequencies, or, in other words, to solve Maxwell's equations (6). These equations are numerically solved using the 3-D EM forward modeling code PGIEM2G (Kruglyakov & Kuvshinov, 2018), which is based on a method of volume integral equations (IE) with a contracting kernel (Pankratov & Kuvshinov, 2016). PGIEM2G exploits a piece-wise polynomial basis; in this study, PGIEM2G was run using the first-order polynomials in lateral directions and third-order polynomials in the vertical direction.

Figures 11, 12, and 13 demonstrate $\mathbf{E}_i(\mathbf{r}_s, \omega; \sigma)$ at locations of observatories Abisko (ABK), Uppsala (UPS), and Saint Petersburg (SPG), respectively. The results are for the excitations corresponding to the first, seventh, fourteenth and twenty-first spatial modes and are shown for the frequency range from 10^{-5} Hz to 1 Hz. From these figures, a few observations can be made. The behavior of $\mathbf{E}_i$ (with respect to frequency) varies with location and mode. Real and imaginary parts of $\mathbf{E}_i$ are comparable in magnitude. As

expected, $\mathbf{E}_i$ are smooth functions with respect to the frequency; apparent non-smoothness of the results in some plots is due to the fact that *absolute* values of real and imaginary parts are shown.

Finally, it is important to note that $\mathbf{E}_i$ decrease – irrespective of the mode and location – as frequency decreases; specifically, the magnitude of $\mathbf{E}_i$ drops down more than two orders of magnitude as frequency decreases from 1 Hz down to 10^{-3} Hz. These plots suggest a value for T in Equation (10); recall, that useful rule of thumb is that the value for T corresponds to the inverse of frequency at which the field becomes small compared to the higher frequencies. Following this rule, $T = 1000$ seconds seems to be a reasonable choice which will be further justified in the next section.

3.4 Model study to justify a value for T

To justify a value for T we first calculate a reference ("true") time-domain electric field for a chosen 8-hours event. This reference field was computed using the procedure presented in Ivannikova et al. (2018); Marshalko et al. (2020, 2021). Specifically, we calculate $\mathbf{j}^{ext}(t, \mathbf{r})$ using Equations (13) and (15) and taking 21 terms in expansion (13). Further, according to Marshalko et al. (2021), we calculate the reference electric field as follows:

1. The source $\mathbf{j}^{ext}(t, \mathbf{r})$ is transformed from the time to the frequency domain with a fast Fourier transform (FFT).

2. Frequency-domain Maxwell's equations (1)-(2) are numerically solved using PGIEM2G at FFT frequencies between $\frac{1}{K}$ and $\frac{1}{2\Delta t}$ where K is the length of the event, and Δt is the sampling rate of the considered time series. In this study Δt is 10 sec, and K is 8 h.

3. $\mathbf{E}(t, \mathbf{r})$ is obtained with an inverse FFT of the frequency-domain field.

Then we calculate electric fields using Equation (11) with $T = 900$ sec (15 min) and with $T = 3600$ sec (1 h) and compare them with the reference field. Figures 11, 12, and 13 show comparison of electric field time series, again, at locations of ABK, UPS and SPG observatories. It is seen that both "real-time" (either calculated using $T =$ 15 min or $T = 1$ h) electric fields agree well with the reference electric field. Tables 1 and 2 confirm this quantitatively by presenting correlation coefficients between corresponding time series and the normalized root-mean-square errors; the latter are defined as

$$\mathrm{nRMSE}(a, b) = \sqrt{\frac{\sum\limits_{i=1}^{N}(a_i - b_i)^2}{N}} \Bigg/ \sqrt{\frac{\sum\limits_{i=1}^{N} b_i^2}{N}}, \tag{21}$$

where a and b are the GEF time series calculated exploiting real-time scheme and the reference GEF time series, respectively, a_i and b_i are elements of these time series, and N is the number of time instants. Since results for $T = 15$ min and $T = 1$ h appear to be very similar, we present in the next section the estimates of computational loads for the case when T is taken as 15 min.

3.5 Computational loads for the real-time GEF calculation

Once $\mathcal{M}^n_{\mathbf{E}_i}(\mathbf{r}_s; \sigma)$ and $\mathcal{L}_i(\mathbf{r}_s, T; \sigma)$ are computed and stored on the disc, GEF at a grid $N_x \times N_y$ and time instant t_k is computed using Equation (11). In accordance with this equation, the GEF calculation requires forcasting/nowcasting the $L \times N_t$ array c, reading the $L \times N_t \times N_g$ array $\mathcal{M}^n_{\mathbf{E}_i}$ and $L \times N_g$ array $\mathcal{L}_i$, and performing $\mathcal{O}(L \times N_t \times N_g)$ summations and multiplications. For our problem setup with $N_g = 512 \times 512$, $N_t =$

90 and $L = 21$ the calculation of $\mathbf{E}(\mathbf{r}_s, t_k; \sigma)$ takes from 0.00625 to 0.025 seconds, depending on the computational environment. Note that to store arrays for this setup one needs 7.25 Gigabytes of disc space.

4 Discussion

4.1 Further justification of the concept

So far, we have demonstrated the concept's validity on an example of a single space weather event. However, one can argue that spatial modes (SM) obtained for a specific event could be non-adequate for other events. To address this question, we performed the following modeling experiment. First, we built the sources for two other space weather events – St. Patrick's Day geomagnetic storm on 17-18 March 2015 and Halloween storm on 29-31 October 2003 – and then approximated corresponding sources using spatial modes obtained for the 7-8 September 2017 storm. To ensure that the spatiotemporal structure of the source for new events is different from that of the (reference) 7-8 September 2017 event, we took the new events' lengths as 48 and 72 h, respectively; recall that the duration of 7-8 September 2017 event was taken as eight hours. Figure 14 shows snapshots of the original and SM-based sources for St. Patrick's Day (top panels) and Halloween (bottom panels) geomagnetic storms. It is seen from the figure that the SM-based source (with SM obtained from another event) approximates very well the source of the other two events. Figure 15 confirms this inference by showing an agreement between the time series of the original and SM-based sources above exemplary site JCK, again, for Halloween (top panels) and St. Patrick's Day (bottom panels) storms. These results suggest that irrespective of the event (which correspond to the sources of different geometry), the spatial structure of these sources is well approximated by a finite number of SM obtained from the analysis of some specific event. The prerequisite to getting adequate SM is that the event to be used for SM estimation should be long enough and sufficiently energetically large and spatially complex.

The linked question we also address is whether $T = 15$ min is a valid choice for the real-time modeling of the GEF during the above discussed events. As in Section 3.4, we calculate electric fields using Equation (11) with $T = 15$ and with $T = 1$ h and compare them with the reference fields. Figures 16 and 17 show the comparison of electric field time series at location of the ABK observatory for Halloween and St. Patrick's Day events, respectively. Similar to the results for 7-8 September 2017 event, both "real-time" (either calculated using $T = 15$ min or $T = 1$ h) electric fields agree well with the reference electric field. Tables 1 and 2 quantify the agreement by presenting correlation coefficients and nRMSE, respectively. It is seen that the agreement between results for two new events is as good as for 7-8 September 2017 geomagnetic storm.

4.2 Nowcasting and forecasting GEF using the proposed concept

In this section we discuss how the proposed concept could be implemented for nowcasting/forecasting of the GEF. Specifically, a scheme to *nowcast* GEF could work as follows:

1. Using magnetic field data collected at an observational network for historical (backward) event/several events one obtains v_i, at $\mathbf{r}_m$. This is done by exploiting the procedure described in Section 3.1. These v_i allow us to represent the source at any time instant t and at any position $\mathbf{r}$ via Equations (13) - (15). In the paper we used IMAGE network of magnetic field data (for 7-8 September 2017 event) to obtain (L = 21) $v_i(\mathbf{r}_m)$ and further $\mathbf{j}_i(\mathbf{r})$. Using IMAGE data, we confine ourselves to Scandinavian region. If the Canada, for example, is a region of interest, one would use the data from the Canadian networks of magnetic field observations, like CARISMA (Mann et al., 2008) and AUTUMNX (Connors et al., 2016).

2. Once $v_i(\mathbf{r}_m)$ and subsequently $\mathbf{j}_i(\mathbf{r})$ are obtained and stored, one estimates electric field at the current time instant, t_k, using Equation (11). This, in particular, requires knowledge of coefficients c_i at time instant t_k and at a number of time instants in the past, $t_k - \Delta t, t_k - 2\Delta t, \ldots, t_k - N_t\Delta t$. The coefficients at these instants are obtained by reusing Equations (16) and (19), namely

$$c_i(t_k - n\Delta t) = \sum_{m=1}^{M} S_m(t_k - n\Delta t)v_i(\mathbf{r}_m), \quad n = 0, 1 \ldots, N_t, \quad i = 1, 2, \ldots, L, \quad (22)$$

where S_m are computed from the available ground magnetic field data. Note that $N_t\Delta t = T$, where T is either 15 min or 1 h in our example. It is also important to stress that for modeling GEF for the next time instant, $t_k+\Delta t$, one needs to update only $c_i(t_k + \Delta t)$.

As for *forecasting* GEF, the scheme could include the following steps:

1. One obtains $v_i(\mathbf{r}_m)$ and subsequently $\mathbf{j}_i(\mathbf{r})$ in a similar manner as it is done in case of nowcasting GEF.
2. One trains the neural network (NN) using as input data the time series of solar wind parameters collected by satellite(s) at L1 Lagrangian point and $c_i(t)$ as output data. Time series $c_i(t)$ for the training period are obtained using Equations (16) and (19). There is a common understanding that the longer time series are used for the training phase, the better the quality of the forecasted results. Therefore, this period preferably should include multiple years of the L1 and ground magnetic field data; recall that $c_i(t)$ during the training phase are obtained from the ground magnetic field data.
3. One forecasts GEF using the trained NN. Ideally, one has to forecast well ahead. However, given observations made at the L1 point, a geomagnetic disturbance is seen on the ground as fast as an hour ahead. This time latency can be further shrunk to half an hour or so, depending on the solar wind speed. This, in particular, advocates real-time modeling GEF which is a topic of this paper.

5 Conclusions

In this paper, we presented a formalism for the real-time computation of the ground electric field (GEF) in a given 3-D Earth's conductivity model excited by a continuously augmented spatially- and temporally-varying source responsible for a space weather event.

The formalism relies on a factorization of the source by spatial modes and time series of respective expansion coefficients, and exploits precomputed frequency-domain GEF generated by corresponding spatial modes.

To validate the formalism, we invoked a high-resolution 3-D conductivity model of Fennoscandia and considered a realistic source built with the use of the SECS method as applied to magnetic field data from the IMAGE network of observations. Factorization of the SECS-recovered source is then performed using the PCA. Eventually, we show that the GEF computation at a given time instant on a 512×512 grid requires at most 0.025 seconds provided that frequency-domain GEF due to the pre-selected spatial modes are computed in advance. This opens a practical opportunity for GEF nowcasting, using ground magnetic field data, or even forecasting, using both ground magnetic field and L1 data.

We illustrate the concept on a Cartesian geometry problem setup. Global-scale implementation is rather straightforward; for this scenario, the source could be obtained either using magnetic field data from a global network of geomagnetic observatories or

exploiting the results of the first-principle modeling of the global magnetosphere-ionosphere system.

Acknowledgments

MK was supported by the New Zealand Ministry of Business, Innovation & Employment through Endeavour Fund Research Programme contract UOOX2002. AK was supported in the framework of Swarm DISC activities, funded by ESA contract no. 4000109587, with the support from EO Science for Society. EM was supported by grant 21-77-30010 from the Russian Science Foundation. The SMAP model is available via the EPOS portal (`http://mt.bgs.ac.uk/EPOSMT/2019/MOD/EPOSMT2019_3D.mod.json`). We thank the institutes that maintain the IMAGE Magnetometer Array: Tromsø Geophysical Observatory of UiT, the Arctic University of Norway (Norway), Finnish Meteorological Institute (Finland), Institute of Geophysics Polish Academy of Sciences (Poland), GFZ German Research Center for Geosciences (Germany), Geological Survey of Sweden (Sweden), Swedish Institute of Space Physics (Sweden), Sodankylä Geophysical Observatory of the University of Oulu (Finland), and Polar Geophysical Institute (Russia). We thank INTERMAGNET (`www.intermagnet.org`) for promoting high standards of magnetic observatory practice.

References

Alken, P., Maute, A., Richmond, A. D., Vanhamäki, H., & Egbert, G. D. (2017). An application of principal component analysis to the interpretation of ionospheric current systems. *Journal of Geophysical Research: Space Physics*, *122*(5), 5687–5708. doi: 10.1002/2017JA024051

Bolduc, L. (2002). GIC observations and studies in the Hydro-Québec power system. *Journal of Atmospheric and Solar-Terrestrial Physics*, *64*(16), 1793–1802. (Space Weather Effects on Technological Systems) doi: 10.1016/S1364-6826(02)00128-1

Connors, M., Schofield, I., Reiter, K., Chi, P. J., Rowe, K. M., & Russell, C. T. (2016). The AUTUMNX magnetometer meridian chain in Québec, Canada. *Earth, Planets and Space*, *68*. doi: 10.1186/s40623-015-0354-4

Dimmock, A. P., Rosenqvist, L., Hall, J.-O., Viljanen, A., Yordanova, E., Honkonen, I., ... Sjöberg, E. C. (2019). The GIC and geomagnetic response over Fennoscandia to the 7-8 September 2017 geomagnetic storm. *Space Weather*, *17*(7), 989–1010. doi: 10.1029/2018SW002132

Dimmock, A. P., Rosenqvist, L., Welling, D., Viljanen, A., Honkonen, I., Boynton, R. J., & Yordanova, E. (2020). On the regional variability of dB/dt and its significance to GIC. *Space Weather*, *18*, e2020SW002497. doi: 10.1029/2020SW002497

Egbert, G. D., Alken, P., Maute, A., Zhang, H., & Richmond, A. D. (2021). Modeling diurnal variation magnetic fields for mantle induction studies. *Geophysical Journal International*. doi: 10.1093/gji/ggaa533

Grayver, A., Kuvshinov, A., & Werthmüller, D. (2021). Time-domain modeling of 3-D Earth's and planetary electromagnetic induction effect in ground and satellite observations. *Journal of Geophysical Research: Space Physics*, e2020JA028672. doi: 10.1029/2020JA028672

Grayver, A., Munch, F. D., Kuvshinov, A. V., Khan, A., Sabaka, T. J., & Tøffner-Clausen, L. (2017). Joint inversion of satellite-detected tidal and magnetospheric signals constrains electrical conductivity and water content of the upper mantle and transition zone. *Geophysical Research Letters*, *44*(12), 6074–6081. doi: 10.1002/2017GL073446

Guzavina, M., Grayver, A., & Kuvshinov, A. (2019). Probing upper mantle electrical conductivity with daily magnetic variations using global to local trans-

fer functions. *Geophysical Journal International*, *219*(3), 2125–2147. doi: 10.1093/gji/ggz412

Honkonen, I., Kuvshinov, A., Rastätter, L., & Pulkkinen, A. (2018). Predicting global ground geoelectric field with coupled geospace and three-dimensional geomagnetic induction models. *Space Weather*, *16*(8), 1028–1041. doi: 10.1029/2018SW001859

Ivannikova, E., Kruglyakov, M., Kuvshinov, A., Rastätter, L., & Pulkkinen, A. (2018). Regional 3-D modeling of ground electromagnetic field due to realistic geomagnetic disturbances. *Space Weather*, *16*(5), 476–500. doi: 10.1002/2017SW001793

Kelbert, A. (2020). The role of global/regional Earth conductivity models in natural geomagnetic hazard mitigation. *Surveys in Geophysics*, *41*, 115–166. doi: 10.1007/s10712-019-09579-z

Korja, T., Engels, M., Zhamaletdinov, A. A., Kovtun, A. A., Palshin, N. A., Smirnov, M. Y., ... BEAR Working Group (2002). Crustal conductivity in Fennoscandia – a compilation of a database on crustal conductance in the Fennoscandian Shield. *Earth, Planets and Space*, *54*, 535–558. doi: 10.1186/BF03353044

Kruglyakov, M., & Kuvshinov, A. (2018). Using high-order polynomial basis in 3-D EM forward modeling based on volume integral equation method. *Geophysical Journal International*, *213*(2), 1387–1401. doi: 10.1093/gji/ggy059

Kuvshinov, A., Grayver, A., Tøffner-Clausen, L., & Olsen, N. (2021). Probing 3-D electrical conductivity of the mantle using 6 years of Swarm, CryoSat-2 and observatory magnetic data and exploiting matrix Q-responses approach. *Earth, Planets and Space*, *73*, 67. doi: 10.1186/s40623-020-01341-9

Love, J. J., Lucas, G. M., Kelbert, A., & Bedrosian, P. A. (2018). Geoelectric hazard maps for the Mid-Atlantic United States: 100 year extreme values and the 1989 magnetic storm. *Geophysical Research Letters*, *45*(1), 5–14. doi: 10.1002/2017GL076042

Mann, I. R., Milling, D. K., Rae, I. J., Ozeke, L. G., Kale, Z. C., Murphy, K. R., ... Singer, H. J. (2008). The upgraded CARISMA magnetometer array in the THEMIS era. *Space Science Reviews*, *141*(1), 413–451. doi: 10.1007/s11214-008-9457-6

Marshalko, E., Kruglyakov, M., Kuvshinov, A., Juusola, L., Kwagala, N. K., Sokolova, E., & Pilipenko, V. (2021). Comparing three approaches to the inducing source setting for the ground electromagnetic field modeling due to space weather events. *Space Weather*, *19*(2), e2020SW002657. doi: 10.1029/2020SW002657

Marshalko, E., Kruglyakov, M., Kuvshinov, A., Murphy, B. S., Rastätter, L., Ngwira, C., & Pulkkinen, A. (2020). Exploring the influence of lateral conductivity contrasts on the storm time behavior of the ground electric field in the eastern United States. *Space Weather*, *18*(3), e2019SW002216. doi: 10.1029/2019SW002216

Pankratov, O., & Kuvshinov, A. (2016). Applied mathematics in EM studies with special emphasis on an uncertainty quantification and 3-D integral equation modelling. *Surveys in Geophysics*, *37*(1), 109–147. doi: 10.1007/s10712-015-9340-4

Püthe, C., & Kuvshinov, A. (2013). Towards quantitative assessment of the hazard from space weather. Global 3-D modellings of the electric field induced by a realistic geomagnetic storm. *Earth, Planets and Space*, *65*, 1017–1025. doi: 10.5047/eps.2013.03.003

Rosenqvist, L., & Hall, J. O. (2019). Regional 3-D modeling and verification of geomagnetically induced currents in Sweden. *Space Weather*, *17*(1), 27–36. doi: 10.1029/2018SW002084

Sun, J., & Egbert, G. D. (2012). Spherical decomposition of electromagnetic fields

generated by quasi-static currents. *GEM - International Journal on Geomathematics*, *3*(2), 279–295. doi: 10.1007/s13137-012-0039-0

Svetov, B. S. (1991). Transfer functions of the electromagnetic field (in Russian). *Fizika Zemli*, *1*, 119–128.

Tanskanen, E. I. (2009). A comprehensive high-throughput analysis of substorms observed by IMAGE magnetometer network: Years 1993–2003 examined. *Journal of Geophysical Research: Space Physics*, *114*(A5). doi: 10.1029/2008JA013682

Tasistro-Hart, A., Grayver, A., & Kuvshinov, A. (2021). Probabilistic geomagnetic storm forecasting via deep learning. *Journal of Geophysical Research: Space Physics*, *126*(1), e2020JA028228. doi: 10.1029/2020JA028228

Vanhamäki, H., & Juusola, L. (2020). Introduction to Spherical Elementary Current Systems. In M. W. Dunlop & H. Lühr (Eds.), *Ionospheric multi-spacecraft analysis tools: Approaches for deriving ionospheric parameters* (pp. 5–33). Cham: Springer International Publishing. doi: 10.1007/978-3-030-26732-2_2

Werthmüller, D., Key, K., & Slob, E. C. (2019). A tool for designing digital filters for the Hankel and Fourier transforms in potential, diffusive, and wavefield modeling. *Geophysics*, *84*(2), F47–F56. doi: 10.1190/geo2018-0069.1

Zenhausern, G., Kuvshinov, A., Guzavina, M., & Maute, A. (2021). Towards probing Earth's upper mantle with daily magnetic field variations: exploring a physics-based parametrization of the source. *Earth, Planets and Space*, *73*, 136. doi: 10.1186/s40623-021-01455-8

Appendix A Properties of transfer functions and impulse responses

The convolution integrals in Equation (9) represent the response of the medium to a time-varying extraneous current. These relations follow from the properties of a physical system we consider. We list these properties below and discuss implications. The presentation closely follows a more detailed analysis by Svetov (1991). Note that for the sake of clarity, we discuss the properties on an example of abstract scalar quantities and omit their dependence on spatial variables and electrical conductivity pertinent to our application.

1. **Linearity** allows us to define a response, $\zeta(t)$, of the medium at time t to an extraneous forcing as
$$\zeta(t) = \int_{-\infty}^{\infty} \mathcal{F}(t,t')\chi(t')dt', \tag{A1}$$
where χ is the extraneous forcing that depends on time t' and $\mathcal{F}(t,t')$ is the medium Green's function.
2. **Stationarity** implies that the response of the medium does not depend on the time of occurrence of the excitation. In this case $\mathcal{F}(t,t') \equiv f(t-t')$ and eq. (A1) is rewritten as a convolution integral
$$\zeta(t) = \int_{-\infty}^{\infty} f(t-\tau)\chi(\tau)d\tau = \int_{-\infty}^{\infty} f(\tau)\chi(t-\tau)d\tau, \tag{A2}$$
where $f(t)$ represents the impulse response of the medium. In the frequency domain, the convolution integral degenerates to
$$\tilde{\zeta}(\omega) = \tilde{f}(\omega)\tilde{\chi}(\omega), \tag{A3}$$
where $\tilde{f}(\omega)$ is called the transfer function and we use tilde sign ($\tilde{\cdot}$) to denote complex-valued quantities. Equations (A2) and (A3) are related through the Fourier trans-

form

$$\tilde{f}(\omega) = \int_{-\infty}^{\infty} f(t) e^{\mathrm{i}\omega t} \mathrm{d}t. \tag{A4}$$

3. Since we work in the time domain with a real-valued forcing, the impulse response is also **real**. To see implications of this, let us define the inverse Fourier transform of $\tilde{f}(\omega) = f_R(\omega) + \mathrm{i} f_I(\omega)$ as

$$\begin{aligned} f(t) &= \frac{1}{2\pi} \int_{-\infty}^{\infty} \tilde{f}(\omega) e^{-\mathrm{i}\omega t} \mathrm{d}\omega \\ &= \frac{1}{2\pi} \int_{-\infty}^{\infty} \left[f_R(\omega) \cos(\omega t) + f_I(\omega) \sin(\omega t) \right] \mathrm{d}\omega \\ &+ \frac{\mathrm{i}}{2\pi} \int_{-\infty}^{\infty} \left[f_I(\omega) \cos(\omega t) - f_R(\omega) \sin(\omega t) \right] \mathrm{d}\omega, \end{aligned} \tag{A5}$$

For an impulse response to be real, the last term in the integral (A5) has to vanish. This is possible only if $f_R(\omega)$ and $f_I(\omega)$ are even and odd functions of ω, respectively. Therefore, Equation (A5) reduces to

$$f(t) = \frac{1}{\pi} \int_{0}^{\infty} \left[f_R(\omega) \cos(\omega t) + f_I(\omega) \sin(\omega t) \right] \mathrm{d}\omega. \tag{A6}$$

4. Impulse response is **causal**. This property implies that

$$f(t) = 0, \qquad t < 0. \tag{A7}$$

Under this assumption, the convolution integral (A2) is recast to

$$\zeta(t) = \int_{0}^{\infty} f(\tau) \chi(t-\tau) d\tau = \int_{-\infty}^{t} f(t-\tau) \chi(\tau) d\tau. \tag{A8}$$

Also, due to causality (cf. Equation A7), and exploiting Equation (A6), one can write for $t < 0$

$$\frac{1}{\pi} \int_{0}^{\infty} f_R(\omega) \cos(\omega t) \mathrm{d}\omega = -\frac{1}{\pi} \int_{0}^{\infty} f_I(\omega) \sin(\omega t) \mathrm{d}\omega, \qquad t < 0. \tag{A9}$$

Further, using the fact that $\cos(\omega t)$ and $\sin(\omega t)$ are odd and even functions with respect of t, one obtains for $t > 0$

$$\frac{1}{\pi} \int_{0}^{\infty} f_R(\omega) \cos(\omega t) \mathrm{d}\omega = \frac{1}{\pi} \int_{0}^{\infty} f_I(\omega) \sin(\omega t) \mathrm{d}\omega, \qquad t > 0. \tag{A10}$$

Using the latter equation and Equation (A6) one can state that the impulse response is determined by using either only real or imaginary part of $\tilde{f}(\omega)$:

$$f(t) = \frac{2}{\pi} \int_{0}^{\infty} f_R(\omega) \cos(\omega t) \mathrm{d}\omega = \frac{2}{\pi} \int_{0}^{\infty} f_I(\omega) \sin(\omega t) \mathrm{d}\omega, \qquad t > 0. \tag{A11}$$

Appendix B Details of the numerical computation of the real-time GEF

As discussed in the main text, to calculate the GEF in near-real time one needs to efficiently estimate integrals in the right-hand side (RHS) of the equation below

$$\mathbf{E}(\mathbf{r}_s,t;\sigma)=\sum_{i=1}^{L}\int_0^{\infty}c_i(t-\tau)\mathbf{E}_i(\mathbf{r}_s,\tau;\sigma)\mathrm{d}\tau\approx\sum_{i=1}^{L}\int_0^{T}c_i(t-\tau)\mathbf{E}_i(\mathbf{r}_s,\tau;\sigma)\mathrm{d}\tau. \tag{B1}$$

With finite T, one must account for a possibly substantial linear trend in time series $c_i(t)$. By removing the trend, we are forced to work with the following function

$$d_i(t,\tau;T)=\begin{cases}c_i(t-\tau)-c_i(t)-\dfrac{c_i(t-T)-c_i(t)}{T}\tau, & \tau\in[0,T]\\ 0, & \tau\notin[0,T].\end{cases} \tag{B2}$$

Substituting Equation (B2) into the RHS of Equation (B1), and considering (for simplicity) only one term in the sum, we obtain

$$\begin{aligned}&\int_0^{T}c_i(t-\tau)\mathbf{E}_i(\mathbf{r}_s,\tau;\sigma)d\tau=c_i(t)\int_0^{T}\mathbf{E}_i(\mathbf{r}_s,\tau;\sigma)d\tau+\\ &\int_0^{T}d_i(t,\tau;T)\mathbf{E}_i(\mathbf{r}_s,\tau;\sigma)d\tau+\frac{c_i(t-T)-c_i(t)}{T}\int_0^{T}\tau\mathbf{E}_i(\mathbf{r}_s,\tau;\sigma)d\tau.\end{aligned} \tag{B3}$$

Recall that T should be taken large enough to make approximation (B1) valid; particularly, this means that

$$\int_0^{T}\mathbf{E}_i(\mathbf{r}_s,\tau;\sigma)d\tau\approx\int_0^{\infty}\mathbf{E}_i(\mathbf{r}_s,\tau;\sigma)d\tau. \tag{B4}$$

But the integral in the RHS of the latter equation is zero since it corresponds to the electric field generated by the time-constant source. Then, Equation (B3) can be approximated as

$$\int_0^{T}c_i(t-\tau)\mathbf{E}_i(\mathbf{r}_s,\tau;\sigma)d\tau\approx\int_0^{T}d_i(t,\tau;T)\mathbf{E}_i(\mathbf{r}_s,\tau;\sigma)d\tau+[c_i(t-T)-c_i(t)]\,\mathcal{L}_i(\mathbf{r}_s,T;\sigma), \tag{B5}$$

where

$$\mathcal{L}_i(\mathbf{r}_s,T;\sigma)=\frac{1}{T}\int_0^{T}\tau\mathbf{E}_i(\mathbf{r}_s,\tau;\sigma)d\tau. \tag{B6}$$

The integrals $\mathcal{L}_i(\mathbf{r}_s,T;\sigma)$ can be computed using the digital filter technique (see Appendix C), whereas first term in the RHS of Equation (B5) is estimated as follows.

Taking into account that we have $c_i(t)$ at discrete time instants, $t=n\Delta t, n=0,1,\ldots$, we approximate $d_i(t,\tau;T)$ using the Whittaker-Shannon (sinc) interpolation formula

$$d_i(t,\tau;T)\approx\sum_{n=0}^{n\Delta t\le T}d_i(t,n\Delta t;T)\,\mathrm{sinc}\frac{\tau-n\Delta t}{\Delta t}, \tag{B7}$$

where

$$\mathrm{sinc}(x)=\frac{\sin\pi x}{\pi x}. \tag{B8}$$

Recall that sinc interpolation is a method to construct a continuous band-limited function from a sequence of real numbers, in our case time series d_i at time instants $t=n\Delta t, n=$

$0, 1, \ldots$. Note that in our context, the term "band-limited function" means that non-zero values of a Fourier transform of this function are confined to the frequencies

$$|\omega| \leq \frac{\pi}{\Delta t}. \tag{B9}$$

Using the approximation (B7) and taking into account that $\mathbf{E}_i(\mathbf{r}_s, \tau; \sigma) = 0, \tau < 0$ (cf. Appendix A), one obtains

$$\int_0^T d_i(t, \tau; T)\mathbf{E}_i(\mathbf{r}_s, \tau; \sigma)d\tau \approx \int_0^\infty d_i(t, \tau; T)\mathbf{E}_i(\mathbf{r}_s, \tau; \sigma)d\tau = \tag{B10}$$

$$\int_{-\infty}^\infty d_i(t, \tau; T)\mathbf{E}_i(\mathbf{r}_s, \tau; \sigma)d\tau = \sum_{n=0}^{n\Delta t \leq T} d_i(t, n\Delta t; T) \int_{-\infty}^\infty \mathbf{E}_i(\mathbf{r}_s, \tau; \sigma)\,\mathrm{sinc}\frac{\tau - n\Delta t}{\Delta t}d\tau.$$

Thus, we can write

$$\int_0^T d_i(t, \tau; T)\mathbf{E}_i(\mathbf{r}_s, \tau; \sigma)d\tau = \sum_{n=0}^{n\Delta t \leq T} d_i(t, n\Delta t; T)\mathcal{M}^n_{\mathbf{E}_i}(\mathbf{r}_s; \sigma), \tag{B11}$$

where

$$\mathcal{M}^n_{\mathbf{E}_i}(\mathbf{r}_s; \sigma) = \int_{-\infty}^\infty \mathbf{E}_i(\mathbf{r}_s, \tau; \sigma)\,\mathrm{sinc}\frac{\tau - n\Delta t}{\Delta t}d\tau. \tag{B12}$$

Further, following the properties of the Fourier transform as applied to sinc function, we obtain that

$$\mathcal{M}^n_{\mathbf{E}_i}(\mathbf{r}_s; \sigma) = \frac{\Delta t}{2\pi}\int_{-\frac{\pi}{\Delta t}}^{\frac{\pi}{\Delta t}} \mathbf{E}_i(\mathbf{r}_s, \omega; \sigma)e^{-i\omega n\Delta t}d\omega = \mathrm{Re}\left\{\frac{\Delta t}{\pi}\int_0^{\frac{\pi}{\Delta t}} \mathbf{E}_i(\mathbf{r}_s, \omega; \sigma)e^{-i\omega n\Delta t}d\omega\right\}. \tag{B13}$$

Finally, substituting Equation (B11) in Equation (B5), and (B5) in the RHS of (B1) we obtain Equation (11)

$$\mathbf{E}(\mathbf{r}_s, t_k; \sigma) \approx \sum_{i=1}^L \left\{\sum_{n=0}^{N_t} d_i(t_k, n\Delta t; T)\mathcal{M}^n_{\mathbf{E}_i}(\mathbf{r}_s; \sigma) + \left[c_i(t_k - T) - c_i(t_k)\right]\mathcal{L}_i\left(\mathbf{r}_s, T; \sigma\right)\right\},$$

where $d_i(t_k, n\Delta t; T)$, $\mathcal{L}_i\left(\mathbf{r}_s, T; \sigma\right)$, and $\mathcal{M}^n_{\mathbf{E}_i}(\mathbf{r}_s; \sigma)$ are defined in Equations (B2), (B6) and (B13), respectively. Note that the estimation of the integral in the RHS of Equation (B13) is performed using a suitable quadrature formula.

An important note here is that, according to (B13), one does not need to compute $\mathbf{E}_i(\mathbf{r}_s, \omega; \sigma)$ for $\omega > \frac{\pi}{\Delta t}$. This may be obvious, however, this is not the case if one uses piece-wise constant (PWC) approximation of $c_i(t)$ as it is done, for example, in Grayver et al. (2021). With PWC approximation, one is forced to compute the fields at very high frequencies irrespective of Δt value; this can pose a problem from the numerical point of view.

Appendix C Computation of $\mathcal{L}_i(\mathbf{r}_s, T; \sigma)$

With the use of Equation (A11), $\mathbf{E}_i(\mathbf{r}_s, \tau; \sigma)$ can be written as

$$\mathbf{E}_i(\mathbf{r}_s, \tau; \sigma) = \frac{2}{\pi}\int_0^\infty \mathrm{Im}\,\mathbf{E}_i(\mathbf{r}_s, \omega; \sigma)\sin(\omega\tau)\,d\omega. \tag{C1}$$

Substituting the latter equation into Equation (B6) and rearranging the order of integration, we write $\mathcal{L}_i(\mathbf{r}_s, T; \sigma)$ in the following form

$$\mathcal{L}_i(\mathbf{r}_s, T; \sigma) = T \int_0^\infty \Phi(\omega T)\, \mathrm{Im}\, \mathbf{E}_i(\mathbf{r}_s, \omega; \sigma) d\omega, \tag{C2}$$

where $\Phi(\omega T)$ reads

$$\Phi(\omega T) = \frac{2}{\pi} \frac{1}{T^2} \int_0^T \tau \sin(\omega\tau) d\tau = \frac{2}{\pi} \left[\frac{\sin(\omega T)}{(\omega T)^2} - \frac{\cos(\omega T)}{\omega T} \right]. \tag{C3}$$

Integrals in (C2) can be efficiently estimated using the digital filter technique. Specifically, one needs to construct a digital filter for the following integral transform

$$F(T) = T \int_0^\infty \Phi(\omega T) f(\omega) d\omega. \tag{C4}$$

To obtain filter's coefficients for this transform, we exploit the same procedure as in Werthmüller et al. (2019) using the following pair of output and input functions

$$\begin{aligned} F(T) &= \frac{(T+1)e^{-T} - 1}{T}, \\ f(\omega) &= \frac{\omega}{1+\omega^2}. \end{aligned} \tag{C5}$$

Appendix D Formulas for P and Q

The formulas for $P(\mathbf{r}, \mathbf{r}_m)$ and $Q(\mathbf{r}, \mathbf{r}_m)$ (in slightly different notations) are taken from Vanhamäki and Juusola (2020) (see their Sections 2.3 and 2.5) and are as follows

$$P(\mathbf{r}, \mathbf{r}_m) = \frac{\sin C}{4\pi R} \cot \frac{\gamma}{2}, \tag{D1}$$

$$Q(\mathbf{r}, \mathbf{r}_m) = \frac{\cos C}{4\pi R} \cot \frac{\gamma}{2}, \tag{D2}$$

where $R = a + h$, $\mathbf{r} = (R, \vartheta, \varphi)$, $\mathbf{r}_m = (R, \vartheta_m, \varphi_m)$ and γ is an angle between $\mathbf{r}$ and $\mathbf{r}_m$; γ can be determined from the following spherical trigonometry formula

$$\cos\gamma = \cos\vartheta \cos\vartheta_m + \sin\vartheta \sin\vartheta_m \cos(\varphi - \varphi_m), \tag{D3}$$

and $\cos C$ and $\sin C$ are given as

$$\cos C = \frac{\cos\vartheta_m - \cos\vartheta\cos\gamma}{\sin\vartheta\sin\gamma}, \tag{D4}$$

$$\sin C = \frac{\sin\vartheta_m \sin(\varphi_m - \varphi)}{\sin\gamma}. \tag{D5}$$

From Equations (D1) and (D2), it is seen that $P(\mathbf{r}, \mathbf{r}_m)$ and $Q(\mathbf{r}, \mathbf{r}_m)$ tend to infinity as $\mathbf{r}$ tends to $\mathbf{r}_m$. The simplest way to deal with this issue is, as mentioned in Vanhamäki and Juusola (2020), is to consider the grids for $\mathbf{r}$ and $\mathbf{r}_m$ that are shifted with respect to each other. This approach is used in the current paper.

s

Table 1. Correlation coefficients between reference GEF components and GEF components simulated using real-time 3-D GEF modeling approach with 15 min and 1 h time segments at Abisko (ABK), Uppsala (UPS) and Saint Petersburg (SPG) geomagnetic observatories. The results are shown for 3 time intervals: from 20:00:00 UT, 7 September 2017, to 03:59:50 UT, 8 September 2017; from 00:00:00 UT, 17 March 2015, to 23:59:50 UT, 18 March 2015; from 00:00:00 UT, 29 October 2003, to 23:59:50 UT, 31 October 2003.

	ABK	UPS	SPG
2017/09/07 20:00:00 - 2017/09/08 03:59:50			
$\mathrm{corr}(E_{x,15\mathrm{min}},E_{x,\mathrm{ref}})$	0.984	0.991	0.989
$\mathrm{corr}(E_{x,1\mathrm{h}},E_{x,\mathrm{ref}})$	0.984	0.995	0.995
$\mathrm{corr}(E_{y,15\mathrm{min}},E_{y,\mathrm{ref}})$	0.985	0.993	0.983
$\mathrm{corr}(E_{y,1\mathrm{h}},E_{y,\mathrm{ref}})$	0.979	0.997	0.992
2015/03/17 00:00:00 - 2015/03/18 23:59:50			
$\mathrm{corr}(E_{x,15\mathrm{min}},E_{x,\mathrm{ref}})$	0.986	0.992	0.988
$\mathrm{corr}(E_{x,1\mathrm{h}},E_{x,\mathrm{ref}})$	0.986	0.996	0.995
$\mathrm{corr}(E_{y,15\mathrm{min}},E_{y,\mathrm{ref}})$	0.984	0.993	0.983
$\mathrm{corr}(E_{y,1\mathrm{h}},E_{y,\mathrm{ref}})$	0.980	0.997	0.992
2003/10/29 00:00:00 - 2003/10/31 23:59:50			
$\mathrm{corr}(E_{x,15\mathrm{min}},E_{x,\mathrm{ref}})$	0.983	0.991	0.989
$\mathrm{corr}(E_{x,1\mathrm{h}},E_{x,\mathrm{ref}})$	0.984	0.994	0.994
$\mathrm{corr}(E_{y,15\mathrm{min}},E_{y,\mathrm{ref}})$	0.986	0.995	0.989
$\mathrm{corr}(E_{y,1\mathrm{h}},E_{y,\mathrm{ref}})$	0.985	0.997	0.994

Table 2. Normalized root mean square errors calculated based on the reference GEF components and GEF components simulated using real-time 3-D GEF modeling approach with 15 min and 1 h time segments at Abisko (ABK), Uppsala (UPS) and Saint Petersburg (SPG) geomagnetic observatories. The results are shown for 3 time intervals: from 20:00:00 UT, 7 September 2017, to 03:59:50 UT, 8 September 2017; from 00:00:00 UT, 17 March 2015, to 23:59:50 UT, 18 March 2015; from 00:00:00 UT, 29 October 2003, to 23:59:50 UT, 31 October 2003.

	ABK	UPS	SPG
2017/09/07 20:00:00 - 2017/09/08 03:59:50			
nRMSE($E_{x,15\mathrm{min}}$,$E_{x,\mathrm{ref}}$)	0.237	0.167	0.181
nRMSE($E_{x,1\mathrm{h}}$,$E_{x,\mathrm{ref}}$)	0.233	0.128	0.128
nRMSE($E_{y,15\mathrm{min}}$,$E_{y,\mathrm{ref}}$)	0.227	0.147	0.228
nRMSE($E_{y,1\mathrm{h}}$,$E_{y,\mathrm{ref}}$)	0.238	0.112	0.161
2015/03/17 00:00:00 - 2015/03/18 23:59:50			
nRMSE($E_{x,15\mathrm{min}}$,$E_{x,\mathrm{ref}}$)	0.217	0.157	0.179
nRMSE($E_{x,1\mathrm{h}}$,$E_{x,\mathrm{ref}}$)	0.211	0.122	0.122
nRMSE($E_{y,15\mathrm{min}}$,$E_{y,\mathrm{ref}}$)	0.232	0.143	0.214
nRMSE($E_{y,1\mathrm{h}}$,$E_{y,\mathrm{ref}}$)	0.233	0.112	0.158
2003/10/29 00:00:00 - 2003/10/31 23:59:50			
nRMSE($E_{x,15\mathrm{min}}$,$E_{x,\mathrm{ref}}$)	0.231	0.164	0.175
nRMSE($E_{x,1\mathrm{h}}$,$E_{x,\mathrm{ref}}$)	0.224	0.136	0.128
nRMSE($E_{y,15\mathrm{min}}$,$E_{y,\mathrm{ref}}$)	0.215	0.130	0.188
nRMSE($E_{y,1\mathrm{h}}$,$E_{y,\mathrm{ref}}$)	0.213	0.114	0.145

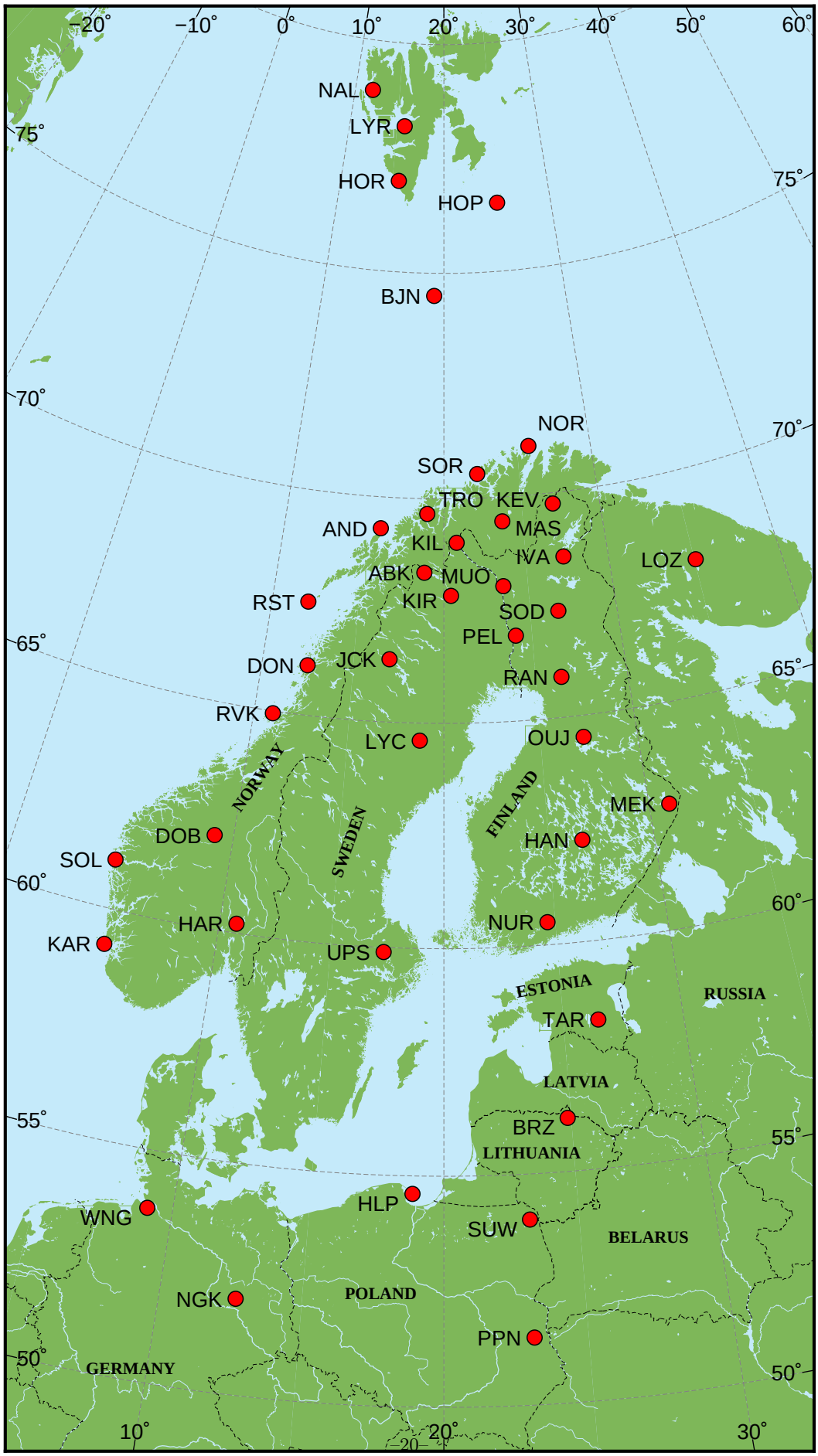

Figure 1. Location of sites from the IMAGE magnetometer network. Credit: Finnish Meteorological Institute.

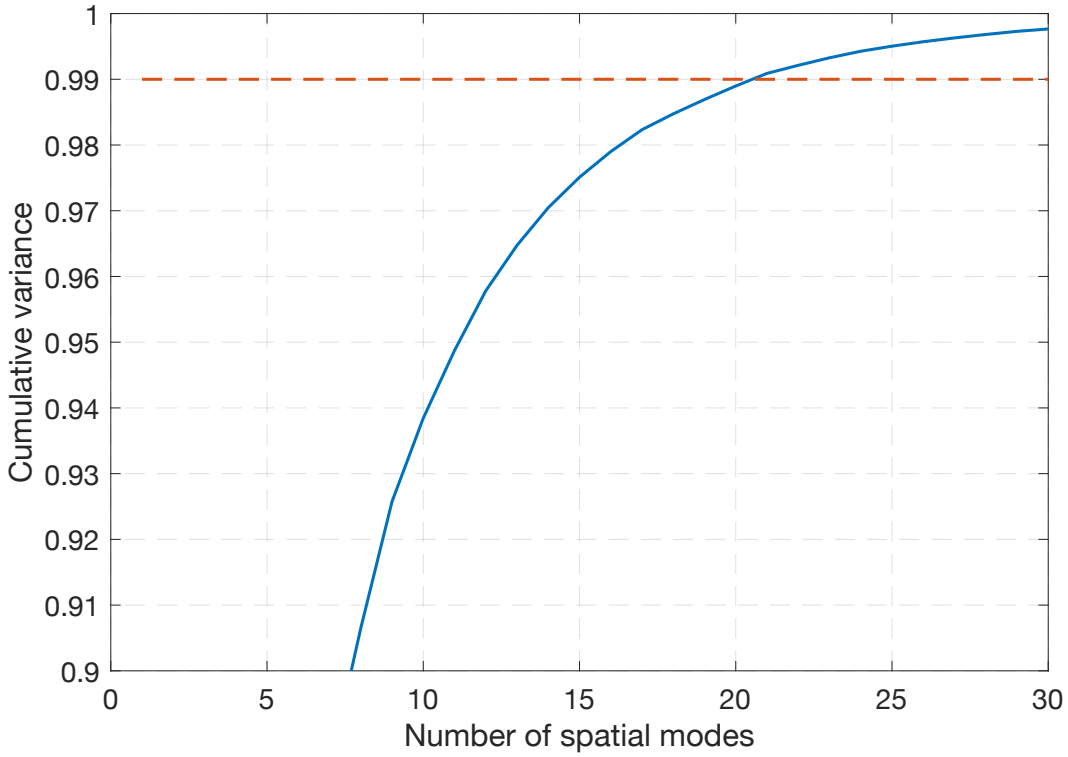

Figure 2. Cumulative variance for the first 30 spatial modes. Red dashed line marks the 99 % threshold.

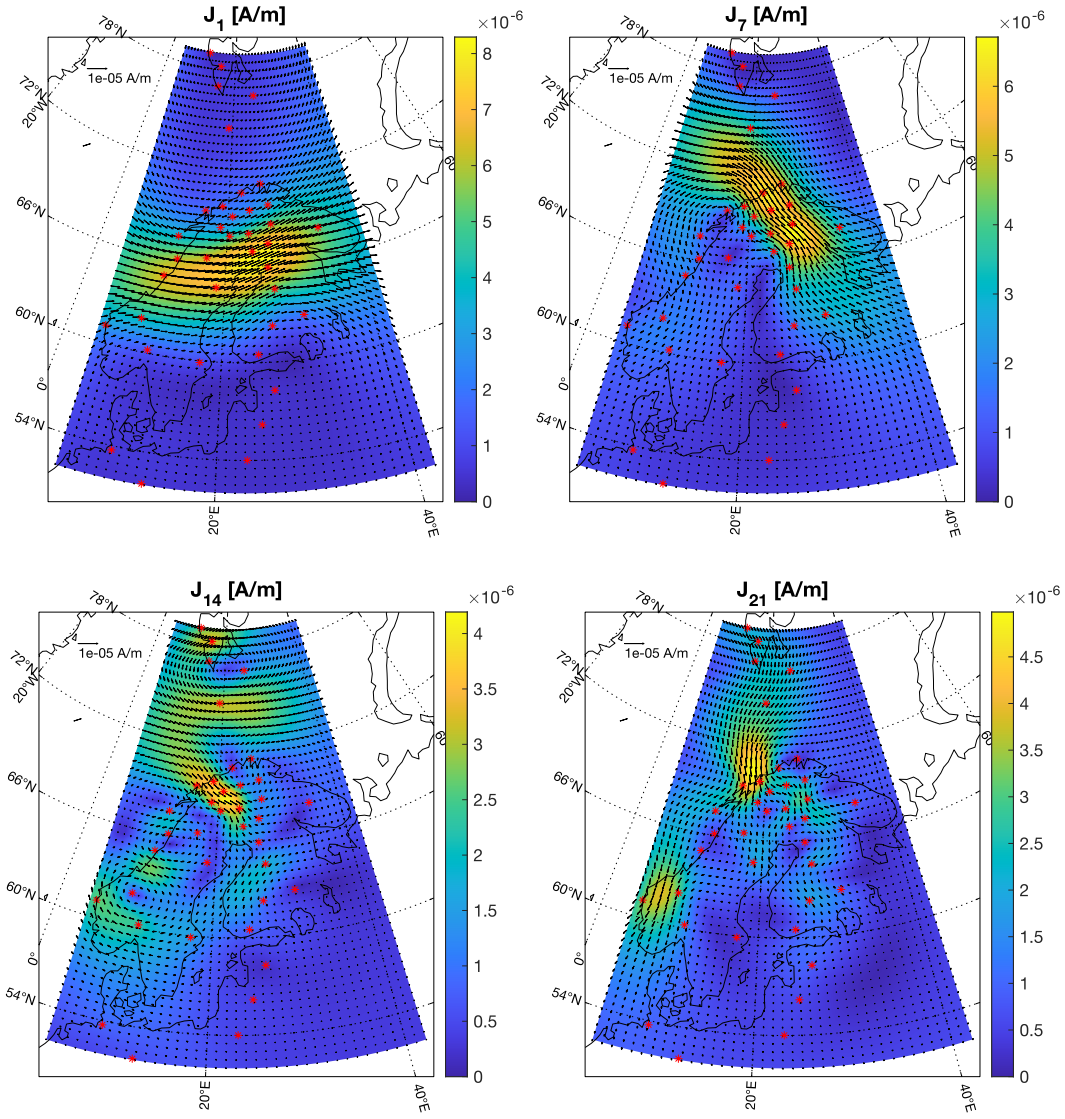

Figure 3. A selection of PCA-recovered $j_i, i = 1, 7, 14, 21$. By colour and arrows, the magnitude (in A/m) and direction of the corresponding j_i are depicted. See details in the text.

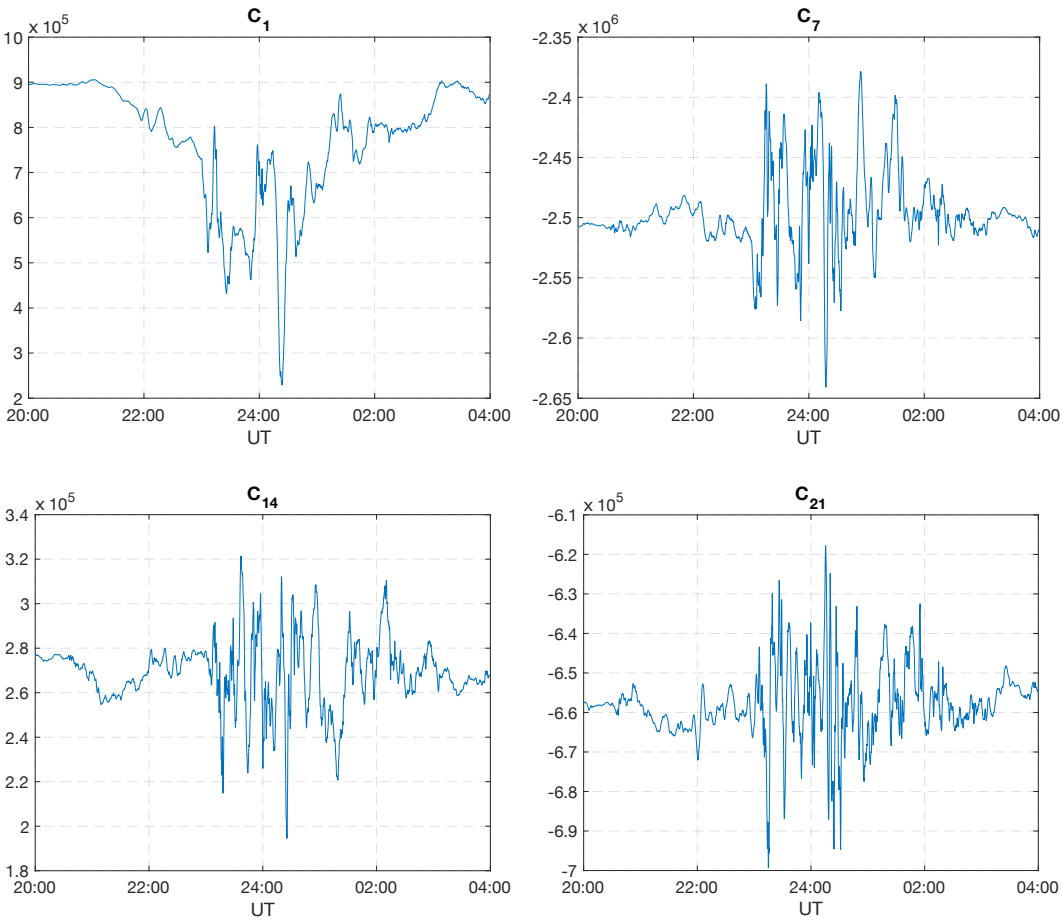

Figure 4. A selection of PCA-recovered $c_i, i = 1, 7, 14, 21$. See details in the text.

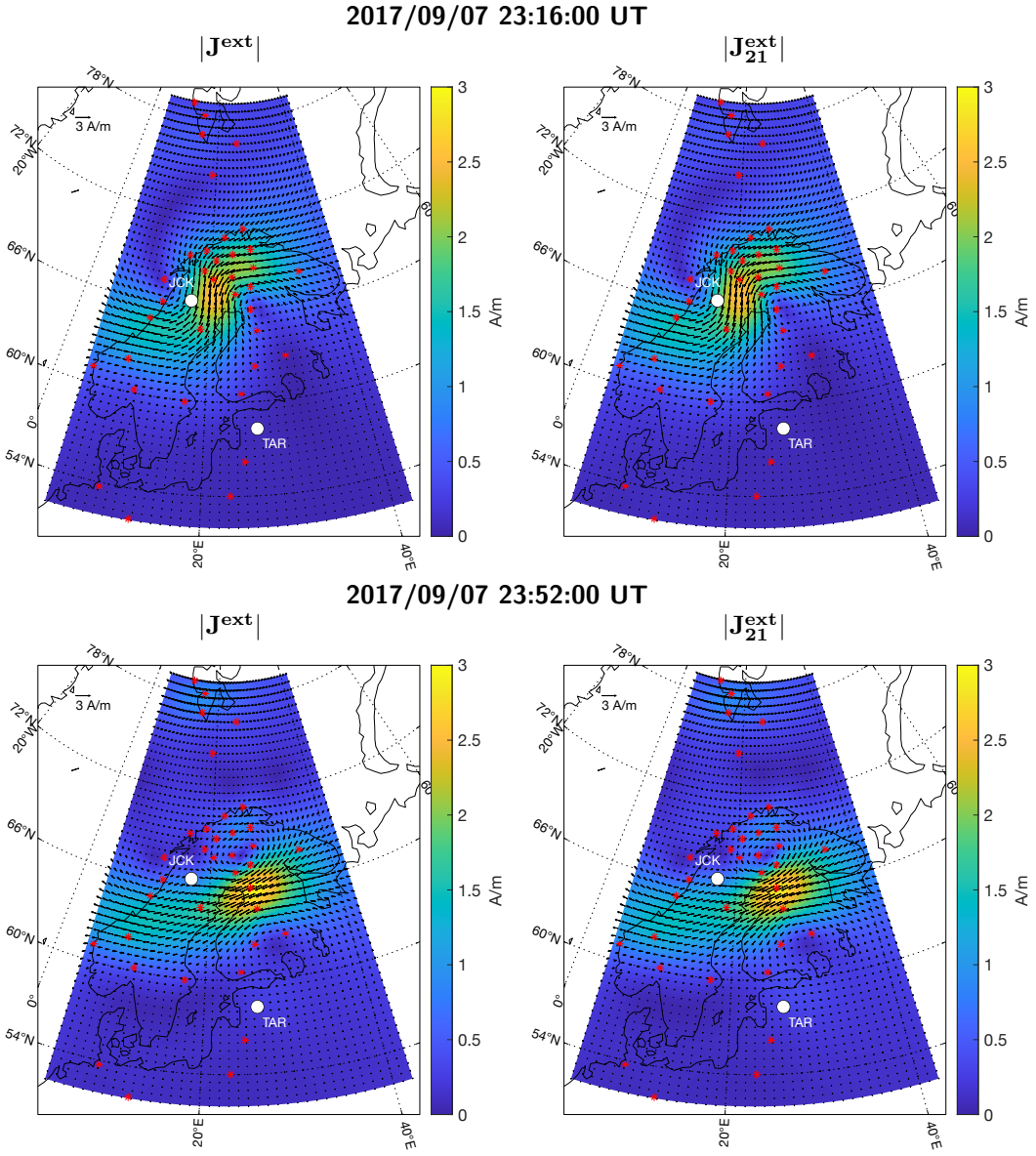

Figure 5. Left: the original external equivalent current. Right: the external equivalent current constructed using 21 spatial modes. The results (in A/m) are for two time instants: 23:16:00 (top row) and 23:52:00 (bottom row) UT on September 7, 2017.

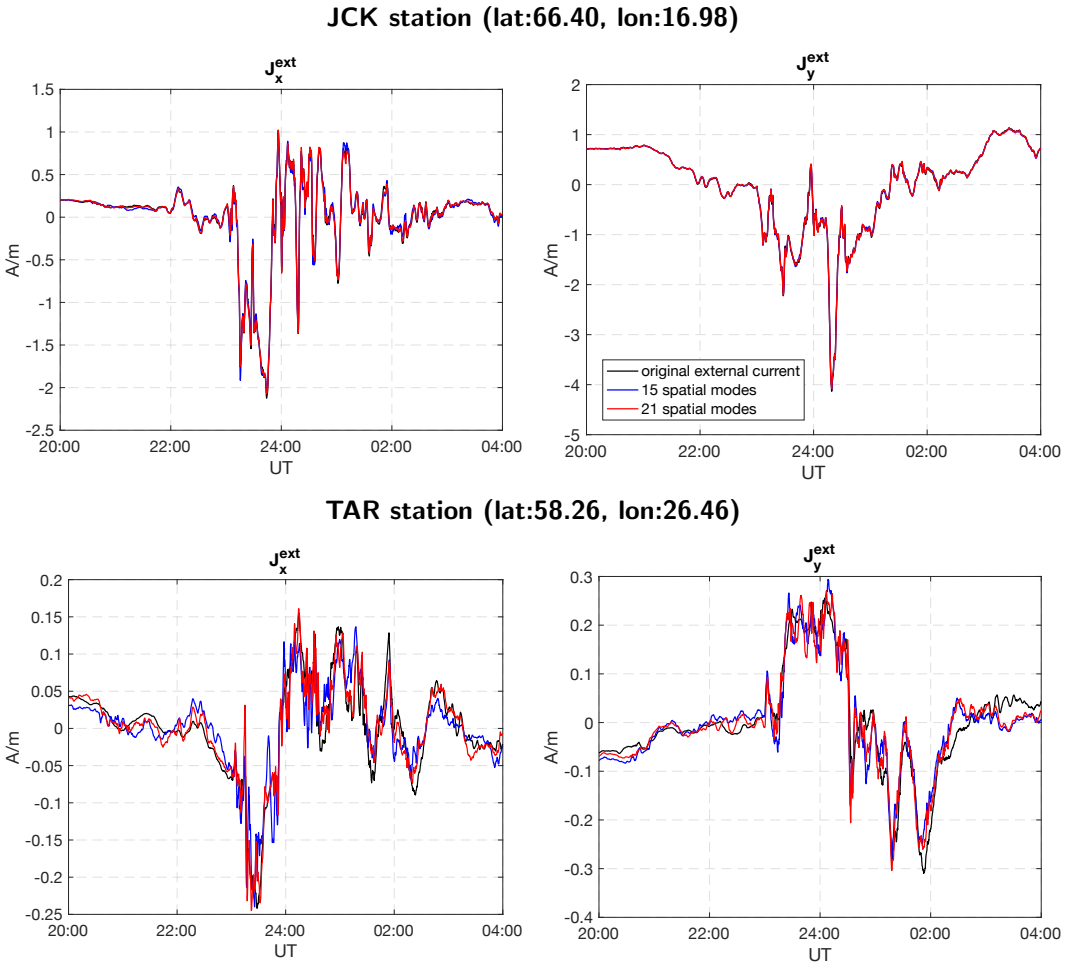

Figure 6. Time series of the original external equivalent current (black curves) and external equivalent current constructed using 15 (blue curves) and 21 spatial modes (red curves) above two exemplary sites (Jäckvik (JCK) and Tartu (TAR)). The results are in A/m. Left and right panels show x- and y-components of the currents, respectively. Note different scales in the panels. Locations of the sites are shown in Figure 5 as white circles.

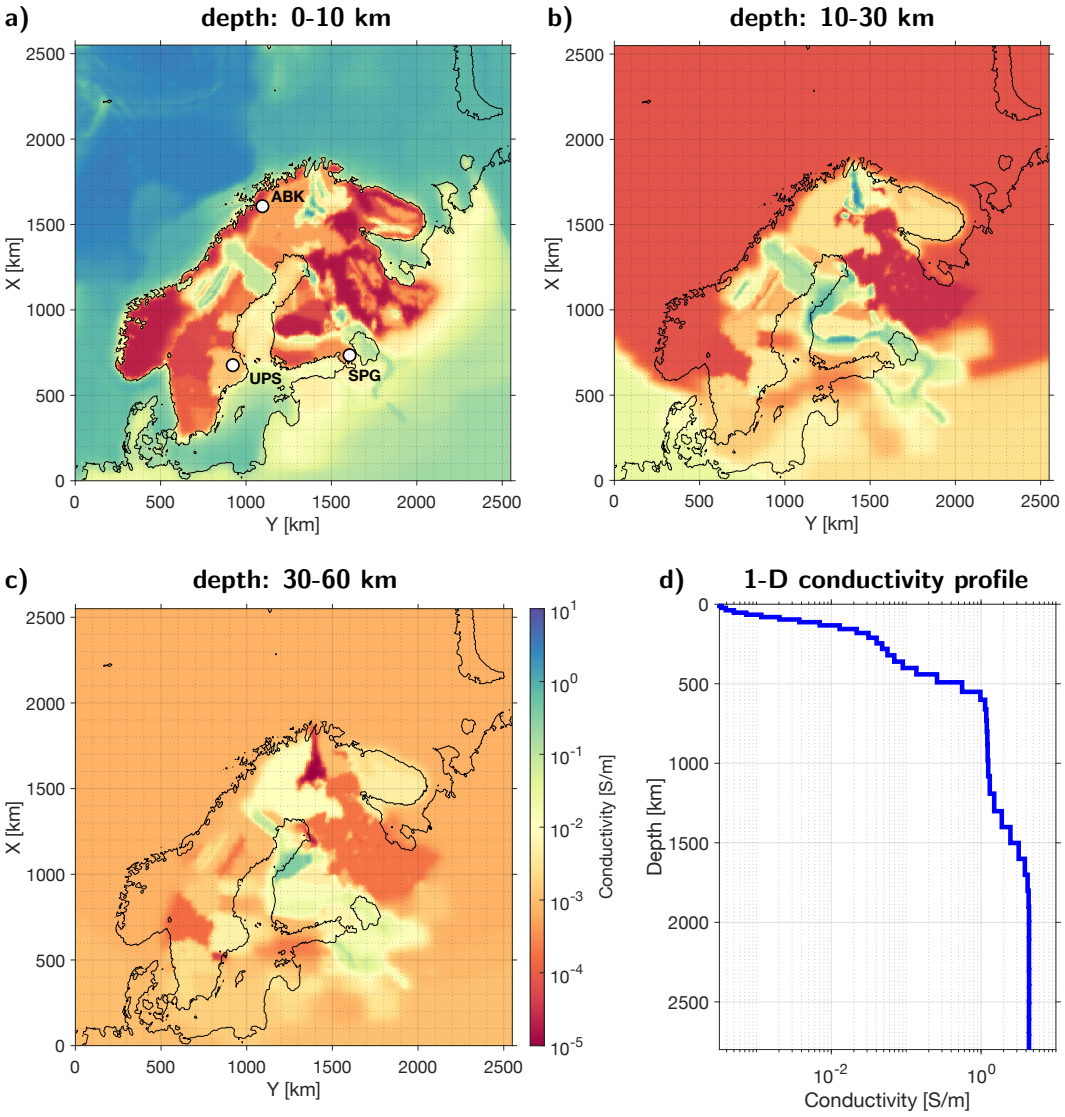

Figure 7. Conductivity distribution [S/m] in the model of Fennoscandia: (a)–(c) Plane view on 3 layers of the 3-D part of the model; (d) global 1-D conductivity profile from Kuvshinov et al. (2021) used in this study. Locations of geomagnetic observatories Abisko (ABK), Uppsala (UPS), and Saint Petersburg (SPG) are marked with circles in plot (a).

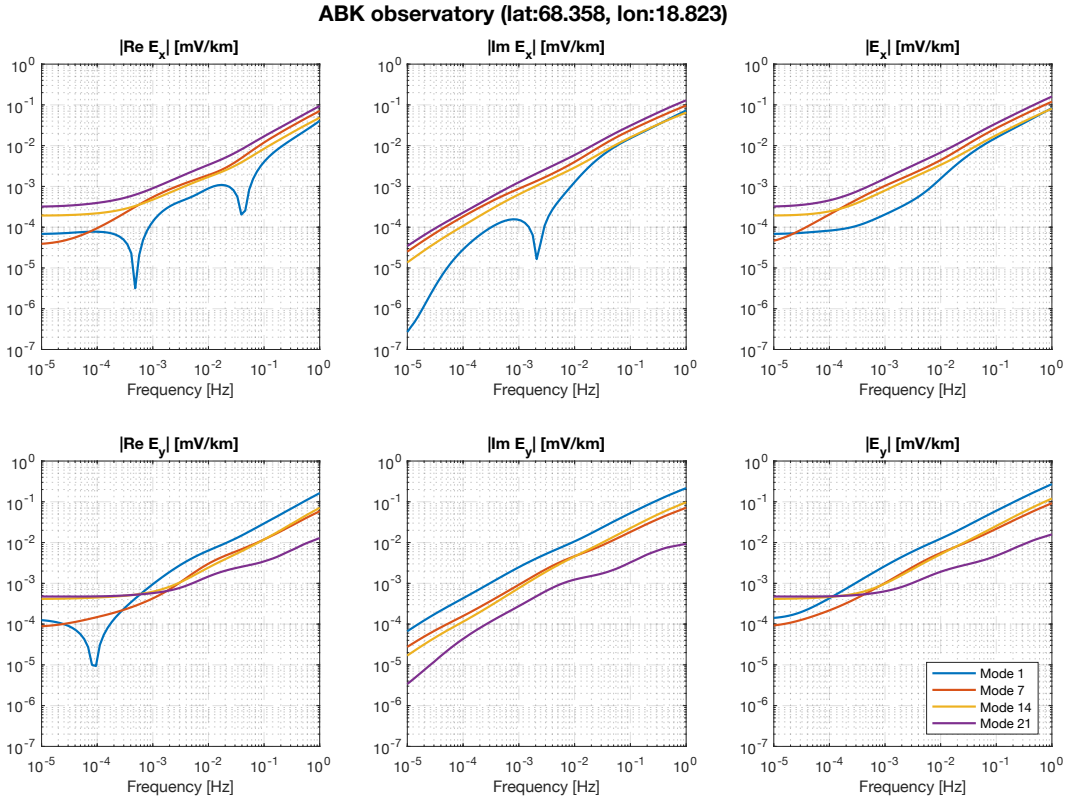

Figure 8. From left to right: absolute values of real part, imaginary part and magnitude of $\mathbf{E}_i(\mathbf{r}_s, \omega; \sigma)$ with respect to frequency, and for a number of spatial modes. Results are for observatory Abisko (ABK) located near the seashore (cf. Fig. 7a). Top and bottom rows show the results for $E_{x,i}$ and $E_{y,i}$ components (in mV/km), respectively.

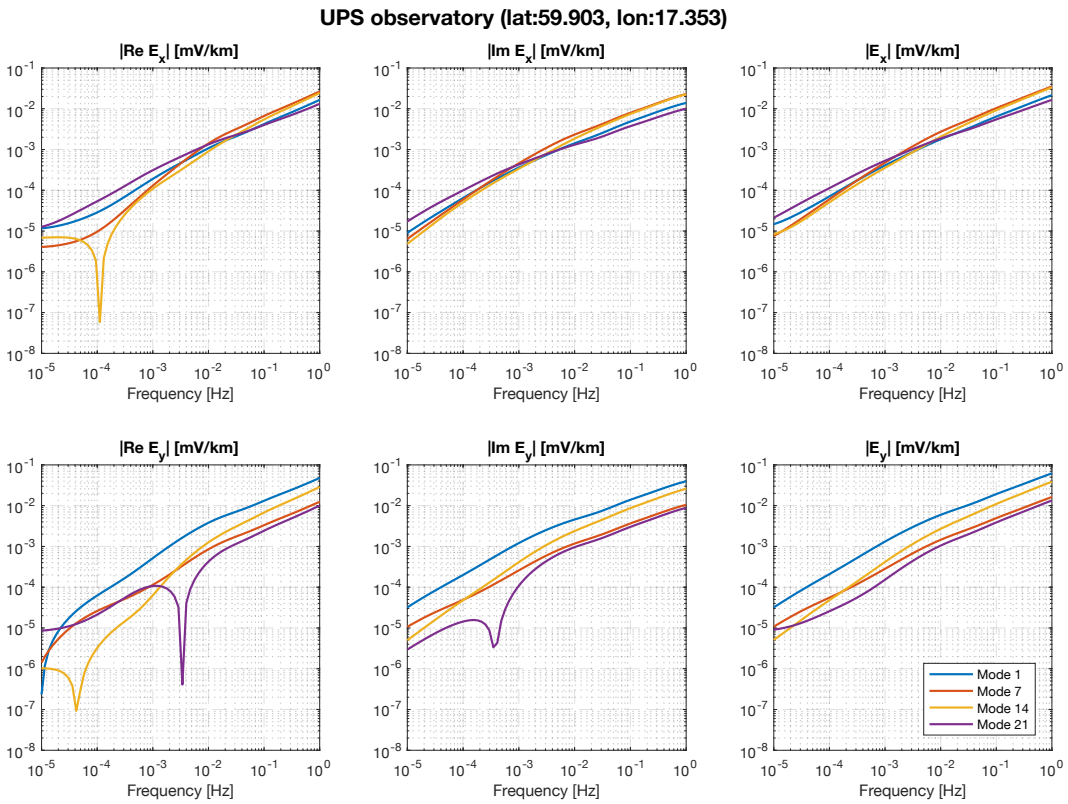

Figure 9. The same caption as in Figure 8 but for inland, Uppsala (UPS), geomagnetic observatory.

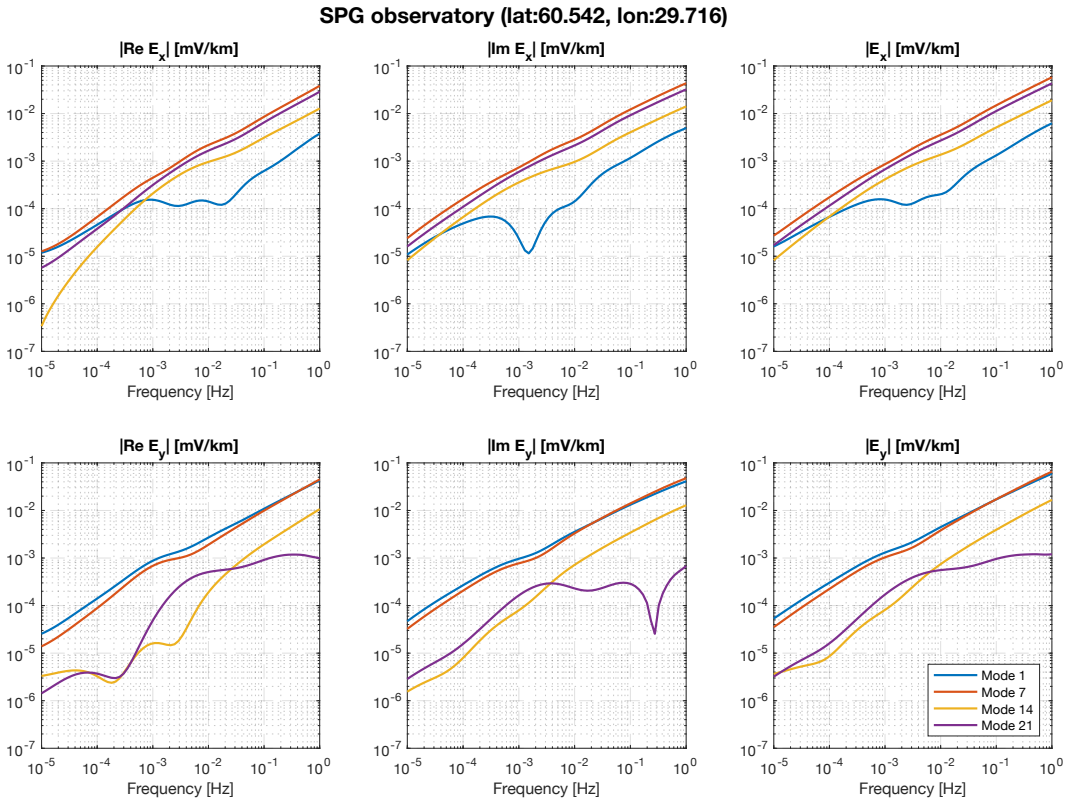

Figure 10. The same caption as in Figure 8 but for Saint Petersburg (SPG) geomagnetic observatory.

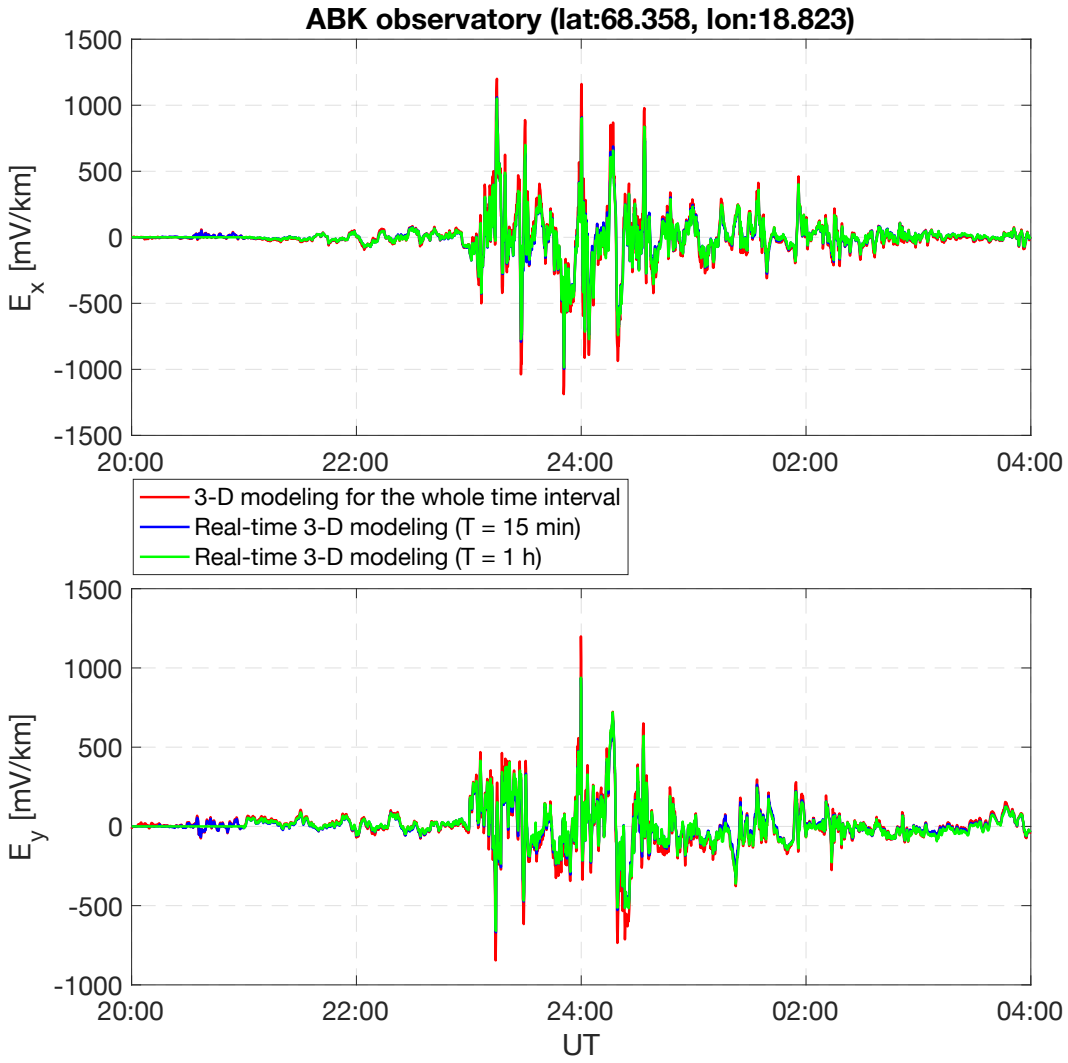

Figure 11. Electric field components at Abisko (ABK) geomagnetic observatory location obtained using 3-D EM modeling with 21 spatial modes for the whole 8 h time interval (from 20:00:00 UT, 7 September 2017, to 03:59:50 UT, 8 September 2017) (red curves) and electric field components at the same observatory simulated using real-time 3-D GEF modeling approach with 15 min (blue curves) and 1 h (green curves) time segments. The results are in mV/km.

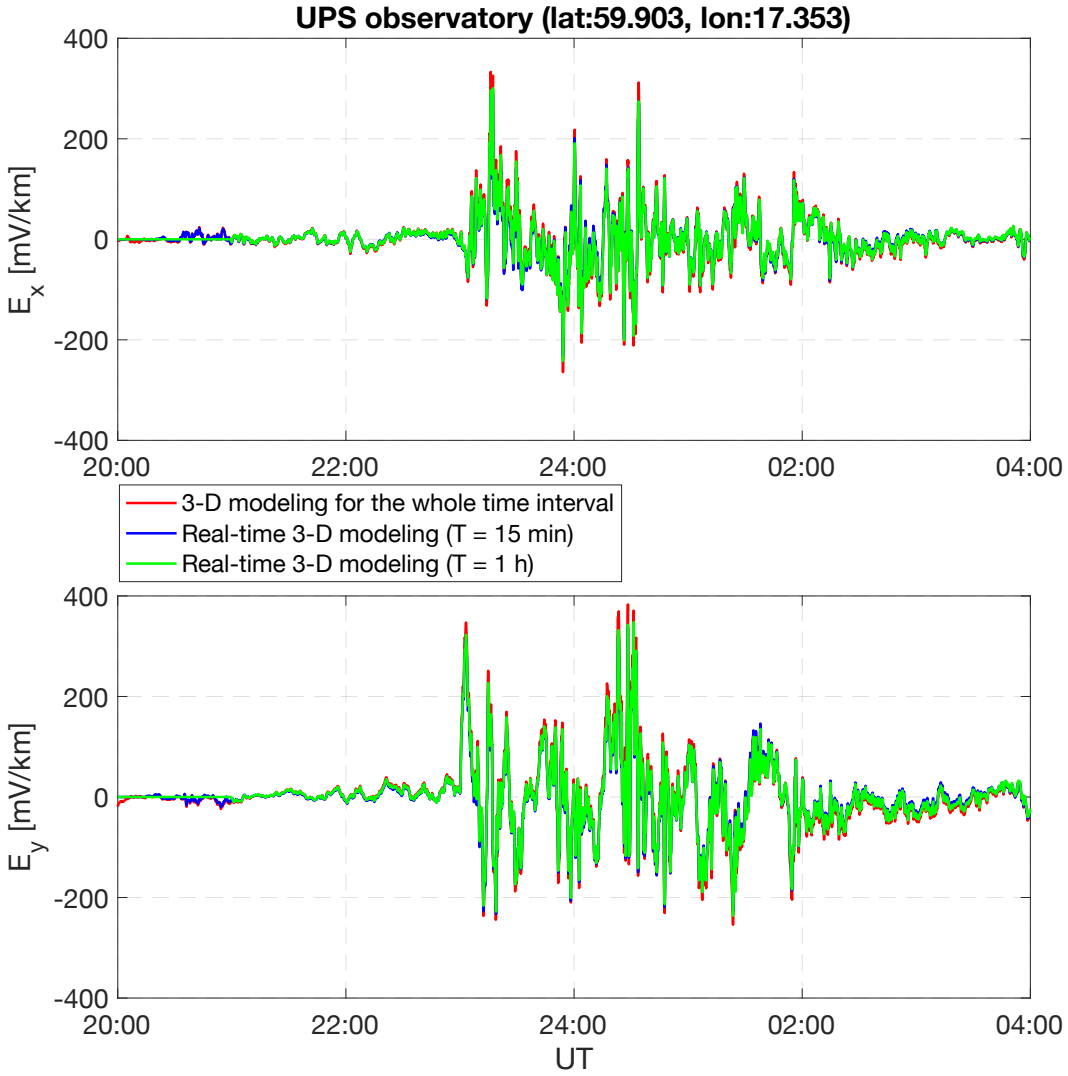

Figure 12. The same caption as in Figure 11 but for Uppsala (UPS) geomagnetic observatory.

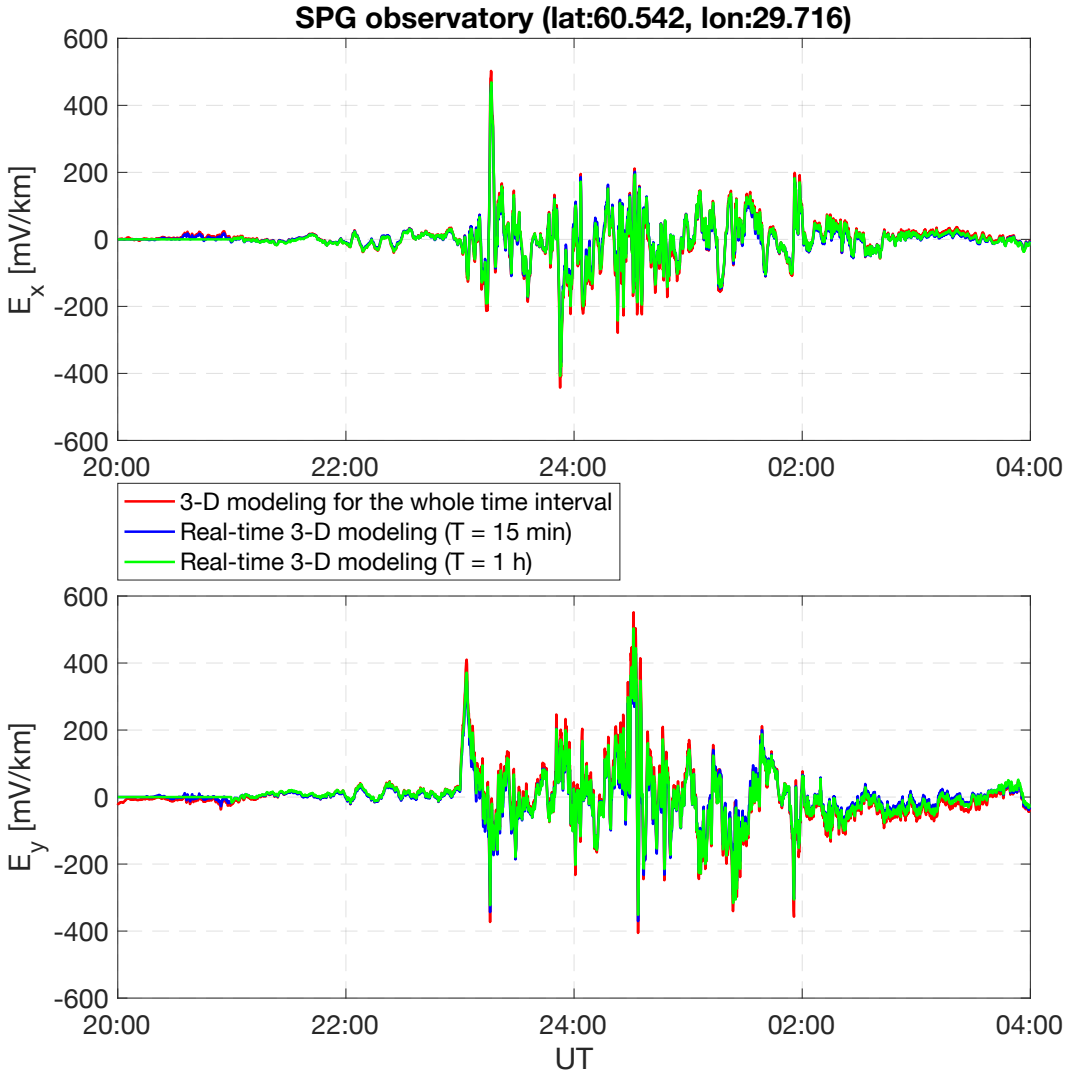

Figure 13. The same caption as in Figure 13 but for Saint Petersburg (SPG) geomagnetic observatory.

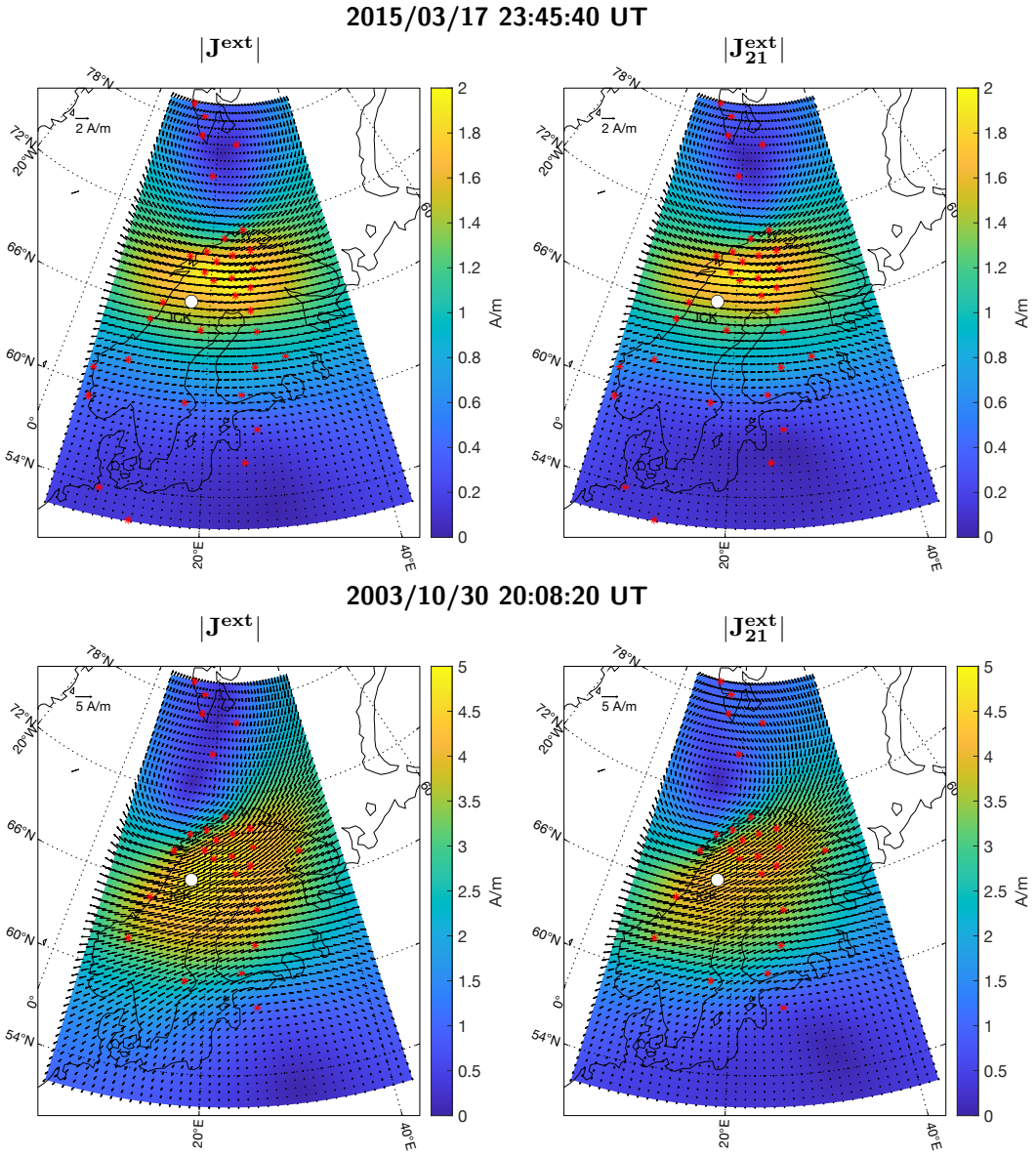

Figure 14. Left: the original external equivalent current. Right: the external equivalent current constructed using 21 spatial modes. The results are for two time instants: 23:45:40 UT on March 17, 2015 (top panels) and 20:08:20 UT on October 30, 2003 (bottom panels). Note that Jäckvik (JCK) site became a part of the IMAGE network on September 1, 2010. Thus, its data were not used for the equivalent current construction in case of the 29-31 October 2003 geomagnetic storm. The results are in A/m.

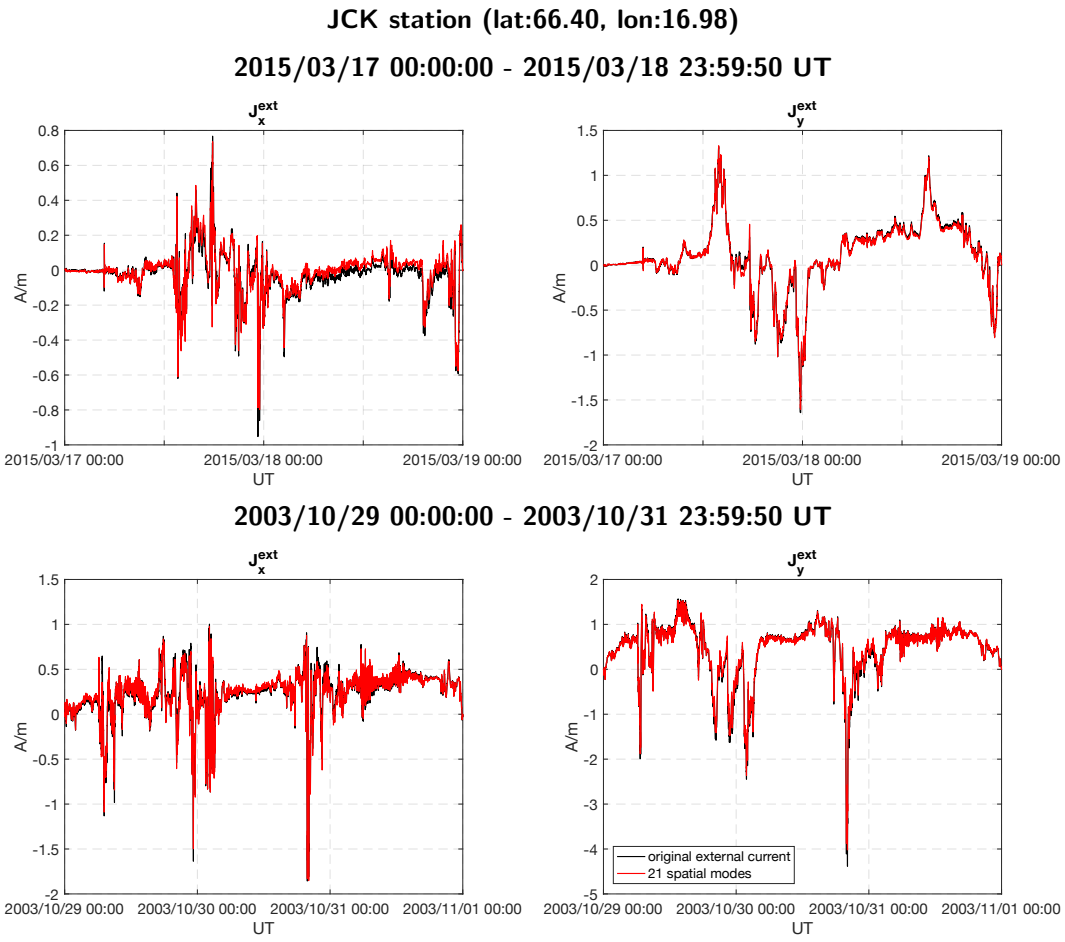

Figure 15. Time series of the original external equivalent current (black curves) and external equivalent current constructed using 21 spatial modes (red curves) above Jäckvik magnetometer (JCK) for two time intervals: from 00:00:00 UT, 17 March 2015, to 23:59:50 UT, 18 March 2015 and from 00:00:00 UT, 29 October 2003, to 23:59:50 UT, 31 October 2003. The location of JCK is shown in Figure 14 as a white circle. Note that JCK magnetometer became a part of the IMAGE network on September 1 2010. Thus, its data were not used for the equivalent current construction in case of the 29-31 October 2003 geomagnetic storm. The results are in A/m.

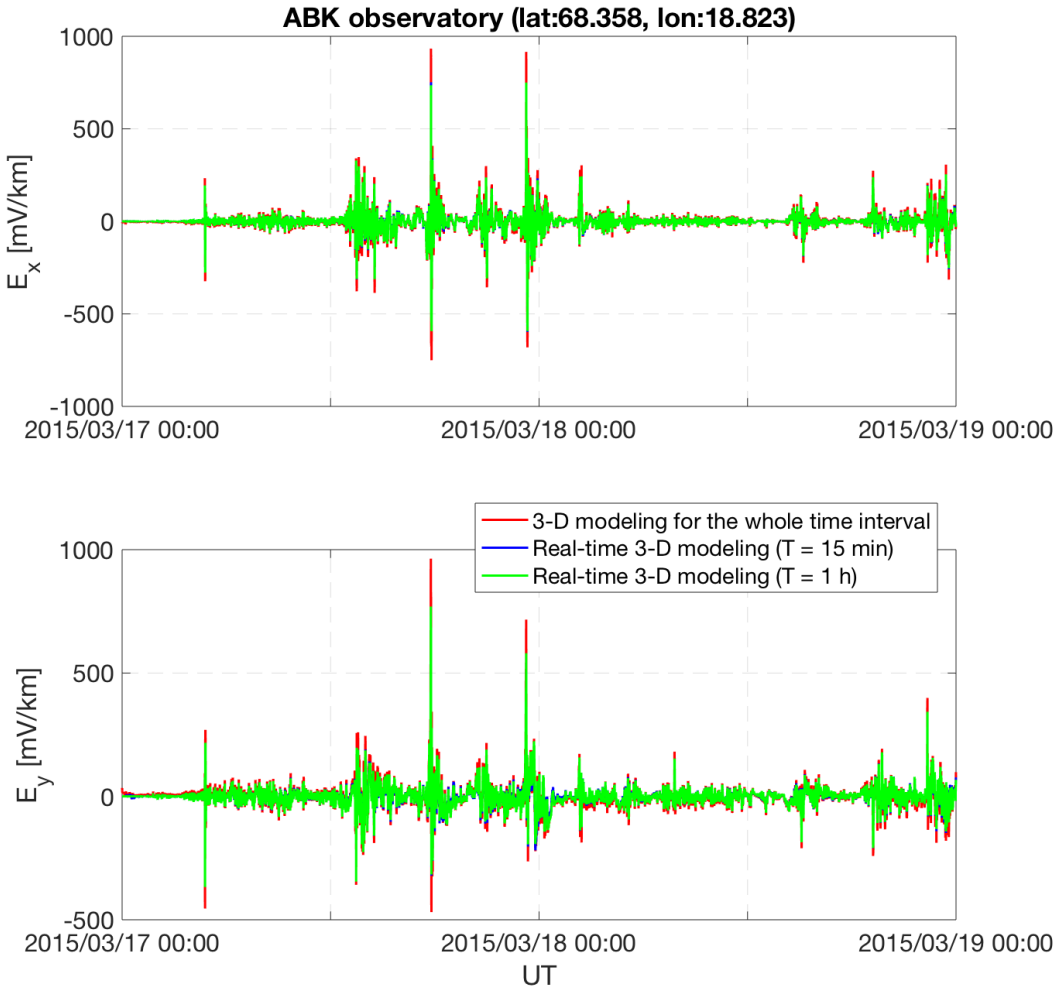

Figure 16. The same caption as in Figure 11 but for a 48 h time interval from 00:00:00 UT, 17 March 2015, to 23:59:50 UT, 18 March 2015.

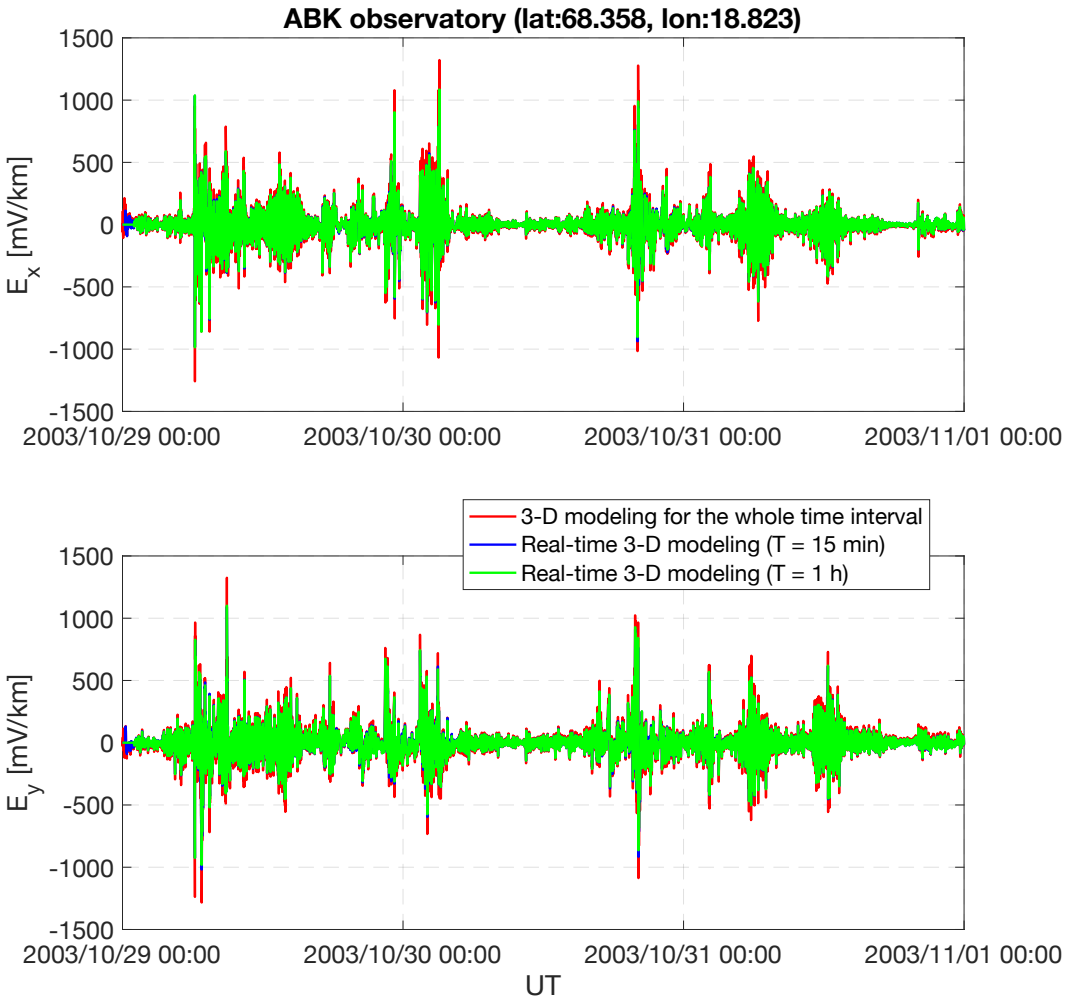

Figure 17. The same caption as in Figure 11 but for a 72 h time interval from 00:00:00 UT, 29 October 2003, to 23:59:50 UT, 31 October 2003.